JULY 1970 N-3C-70-2

GUST PENETRATION LOADS AND ELASTIC VEHICLE RESPONSE FOR SATURN V LAUNCH VEHICLES

Final Technical Report

Prepared by:

Lars E. Ericsson
Senior Staff Engineer, Engineering Technology

J. Peter Reding
Research Specialist, Aero-Thermodynamics

Rolf A. Guenther
Senior Aerodynamics Engineer, Aero-Thermodynamics

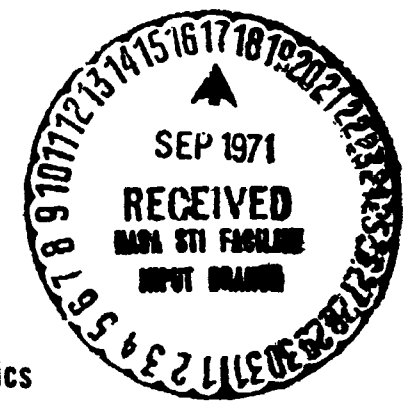

Prepared under Contract NAS 8-21459
For
NASA, George C. Marshall Space Flight Center

Lockheed
MISSILES & SPACE COMPANY
A GROUP DIVISION OF LOCKHEED AIRCRAFT CORPORATION
SUNNYVALE, CALIFORNIA

N-3C-70-2

GUST PENETRATION LOADS AND ELASTIC VEHICLE RESPONSE FOR SATURN V LAUNCH VEHICLES

Final Technical Report

Prepared by
Lars E. Ericsson, J. Peter Reding
and
Rolf A. Guenther

July 1970

Prepared under Contract NAS 8-21459
by Lockheed Missiles & Space Company
for
George C. Marshall Space Flight Center
NATIONAL AERONAUTICS AND SPACE ADMINISTRATION
Huntsville, Alabama

LOCKHEED MISSILES & SPACE COMPANY

ABSTRACT

An analytic study has been made of the gust penetration loads and associated elastic vehicle response of Saturn V launch vehicles penetrating sinusoidal gusts. It is found that the neglect of separated flow effects in existing theories gives highly unrealistic and often unconservative predictions of the gust penetration loads and elastic vehicle response. An analytic theory is presented that includes the effects of separated flow and associated convective time lag effects, and which accepts static experimental data as an input, thereby providing more realistic gust load predictions.

The classical treatment of the high-frequency gust response, e.g., panel vibration, is found to be unrealistic, since it does not include or allow for the effects of large-scale vorticity and coupling between successive separated flow regions.

Saturn V launch vehicles AS-505 through AS-508 were analyzed and found to be aero-elastically stable throughout atmospheric ascent, the only question being whether the predicted large amplitude elastic vehicle bending response to sinusoidal gusts would correspond to structural stresses of tolerable magnitude.

CONTENTS

ILLUSTRATIONS

ILLUSTRATIONS (Continued)

ILLUSTRATIONS (Continued)

SUMMARY

A study of gust penetration loads on Saturn V launch vehicles has produced an analytic theory that, by admitting static experimental data as an input, can give realistic predictions of elastic vehicle gust response including the effects of separated flow and convective flow time lag. It was also found that the available theories for high-frequency gust response, such as panel vibration, were unrealistic as they fail to include the effects of finite scale vortices and coupling between successive separated flow regions. Vehicles AS-505 and AS-508 were found to be aeroelastically stable throughout atmospheric ascent, the only problem being whether the large amplitude response to sinusoidal gusts would generate intolerably high stress levels.

Section 1
INTRODUCTION

The separated flow regions on the Apollo-Saturn launch vehicle generated by the tower-mounted escape rocket and interstage conical fairings can have a dominant influence on the elastic vehicle dynamics (Ref. 1). Because the full-scale vehicle is likely to have undergone design changes after the freeze of the model design, an aeroelastic wind tunnel test can often not be extrapolated to full scale without an analytic theory that includes the combined effects of changed geometry, mode shape, and vehicle trajectory. In view of these difficulties, Marshall Space Flight Center (MSFC) contracted Lockheed Missiles & Space Company (LMSC) to develop the needed analytic means (Contracts NAS 8-5338, NAS 8-11238, and NAS 8-20354).

The quasi-steady-constant-time-lag theory developed by LMSC proved capable of predicting the aeroeleastic characterics measured in the wind tunnel test (Ref. 2). Full-scale characteristics could therefore be predicted with confidence by analytic extrapolation from the wind-tunnel data (Ref. 3). Later checks of the individual separated flow regions showed that the adverse effects of the escape rocket wake on escape vehicle dynamics is well predicted by the LMSC theory (Ref. 4). The steady and unsteady aerodynamic effects of shock-induced boundary-layer separation on cone-cylinder and cylinder-flare bodies have also been studied and are now well understood (Ref. 5).

The report extends the previous analyses and provides the analytic means for the determination of the vehicle response to gust penetration loads, with special emphasis on the effects of sinusoidal gusts. The prediction techniques for attached flow gust penetration loads were reviewed and extended to accommodate inclusion of the effects of free body vortices at high angles of attack (Ref. 6). Special attention was paid to the forcing function introduced by series of shock-boundary layer interactions where

a cascading phenomenon upsets usual axial correlation concepts (Ref. 7). The present report summarizes the results reported in detail in the above interim reports (Refs. 6 and 7). In addition, the aeroelastic characteristics of ascent vehicles AS-505, AS-506, AS-507, and AS-508 were determined (Refs. 8-11). The results are summarized in Appendix B. The results of the gust loads analysis have not been reported earlier. As a consequence, the analysis and its results will be fully described in this report.

Section 2
STATEMENT OF PROBLEM

Flow separation occurs over much of the Apollo-Saturn vehicles (Fig. 1). The multiple regions of flow separation have a dominant influence on the aerodynamic loads (Refs. 1, 2, and 12). Because of the finite convection velocity within the separated flow regions, the effect on the vehicle dynamics is even more dominant, as is illustrated by the damping of an early Apollo-Saturn configuration (Fig. 2 and Ref. 12).

These results indicate that one cannot use attached flow estimates of the aerodynamic loads and expect to get a realistic assessment of elastic vehicle dynamics. Likewise, when considering the gust response of the elastic vehicle, one should not expect realistic results unless the effects of flow separation are properly accounted for. One need only compare an actual load distribution with the potential theory results of Glauz and Blackburn (Ref. 13) to realize the inapplicability of load estimates based upon attached flow (Fig. 3).

This report describes an analytic theory that predicts realistic gust loads for the Apollo-Saturn launch vehicles; i.e., it includes the effects of separated flow.

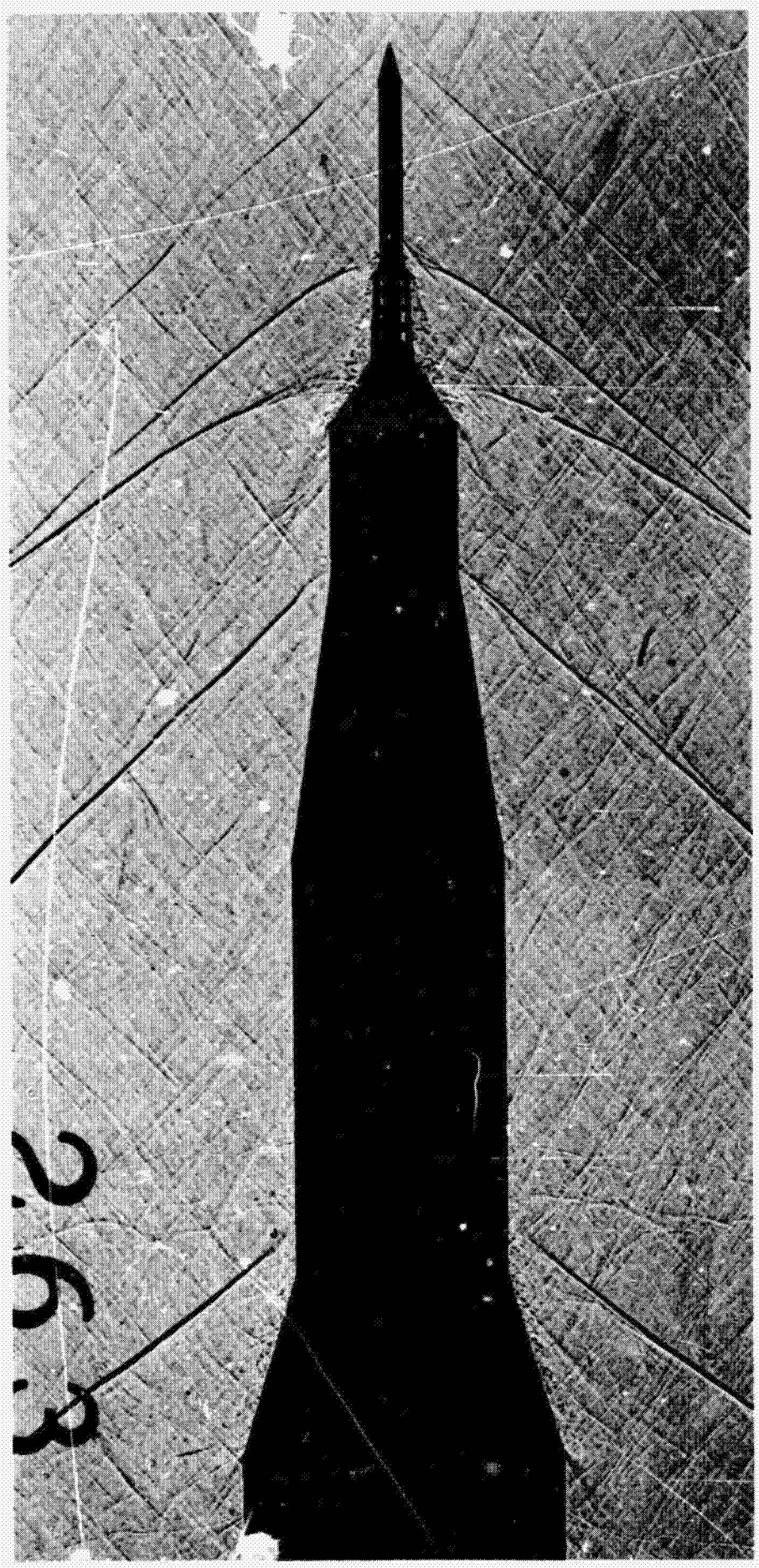

Fig. 1 Shadowgraph of Flo[illegible] V Launch Vehicle at M = 1.46

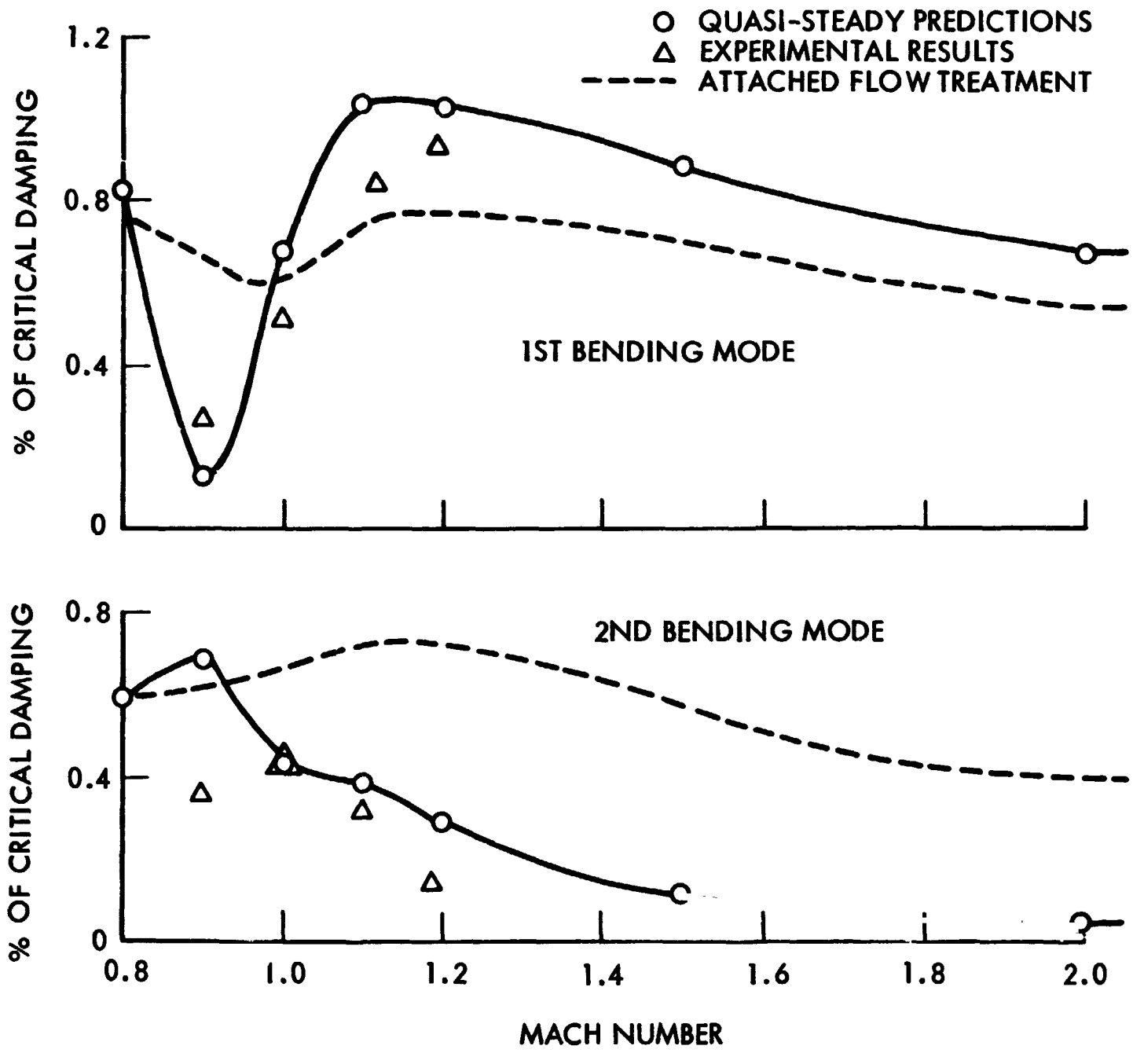

Fig. 2 Aerodynamic Damping at $\alpha = 0$ of Apollo-Saturn I Launch Vehicle with Disk-On Escape Rocket (Ref. 2)

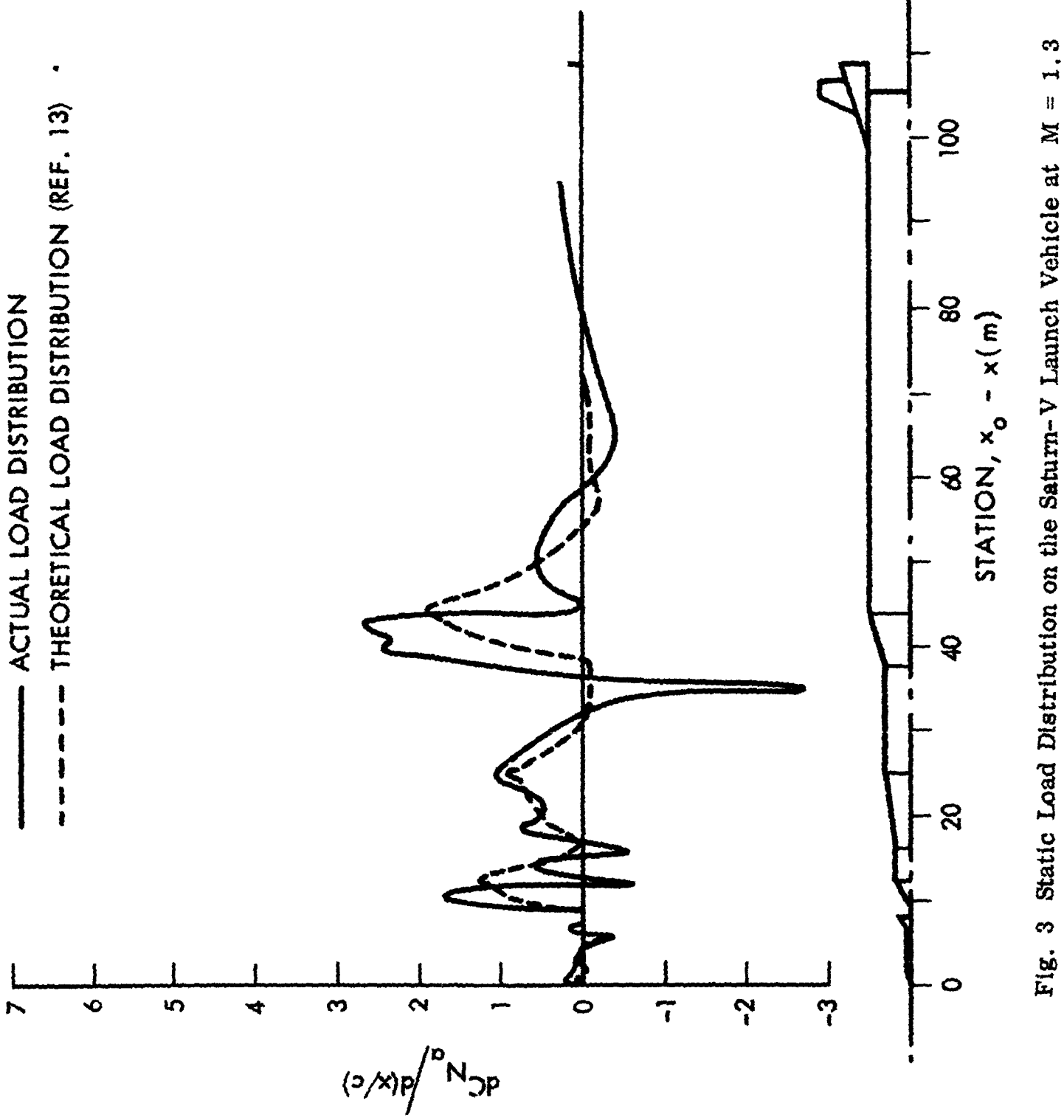

Fig. 3 Static Load Distribution on the Saturn-V Launch Vehicle at M = 1.3

Section 3
ANALYTIC APPROACH

The usual linearization approach is used, i.e., the environment is assumed to change slowly such that the time varying coefficients in the equations of motion can be represented by constant coefficients for finite time intervals in the trajectory. When the full coupled equations of motion are considered this procedure may not always be justified, and the nonlinear equations have to be solved, either by direct numerical techniques (Ref. 14) or by the faster method using perturbation from a reference trajectory (Refs. 15 and 16). Especially when rigid body gust loads are considered the coupling with the control system must be accounted for if meaningful results are to be obtained (Ref. 17).

However, the present analysis is not intended to provide design information for the control system but rather to develop means to assess the effects of gust loads on the structural integrity of the elastic vehicle. Consequently, the gust response can be determined by superposition (Ref. 14). That is, only the linear analysis of one degree of freedom bending response to gust loads will be discussed in this report.

The aerodynamic loads in regions of attached flow are determined by combining first-order momentum theory (Ref. 18) with quasi-steady instantaneous load estimates (Refs. 12 and 19), representing the cruciform fins by an equivalent cross-sectional area distribution (Refs. 12 and 13). The local loads in separated flow regions are represented in a similar manner by an effective cross-sectional area (Refs. 4 and 20). The separation-induced loads are extracted from static experimental data and converted into dynamic loads using quasi-steady techniques that account for convective time lag effects (Refs. 1, 2, 4, and 12).

The gusts are described in the usual manner by a mean wind profile with a small-amplitude perturbation superimposed (Ref. 21); the latter is represented not only by high-frequency atmospheric turbulence, but also by low-frequency discrete harmonics, so-called sinusoidal gusts (Refs. 21 and 22).

Section 4
ANALYSIS

The analysis proceeds as follows: In section 4.1, the gust penetration loads are derived for Apollo-Saturn type launch vehicles, including the effects of the various regions of separated flow. In section 4.2, the single-degree-of-freedom bending response of the elastic vehicle to the gust penetration loads is determined, including the full effects of unsteady aerodynamics, i.e., the separated flow effects on aerodynamic damping are included.

4.1 GUST PENETRATION LOADS

A separated flow region typifying those existing on the Apollo-Saturn launch vehicles is sketched in Fig. 4. The flow is separating at x_N and reattaches at station x_a. The aerodynamic forces in the separated flow region forward of x_a are represented by lumped normal force and axial (force couple) moment vectors. In particular, the normal force N_s and axial force moment M_{A_s} generated on the conical frustum in the separated flow field from the nose is dependent not only upon the local angle of attack, α_s, but also upon the angle of attack α_N at the separated flow generator, the nose, and upon the relative displacement, $y = Y_N - Y_s$, between nose and frustum. For small angles of attack one can write N_s in the following linearized form (a similar expression is obtained for M_{A_s}):

$$N_s = \frac{\rho U^2}{2} S \left\{ \frac{\partial C_{N_s}}{\partial \alpha_s} \alpha_s + \frac{\partial C_{N_s}}{\partial \alpha_N} \alpha_N + \frac{\partial C_{N_s}}{\partial y} y \right\} \qquad (4.1)$$

in the nonstationary case, α_N and Y_N (in $y = Y_N - Y_s$) are the values at a time increment Δt earlier than the instantaneous value for α_s; i.e.,

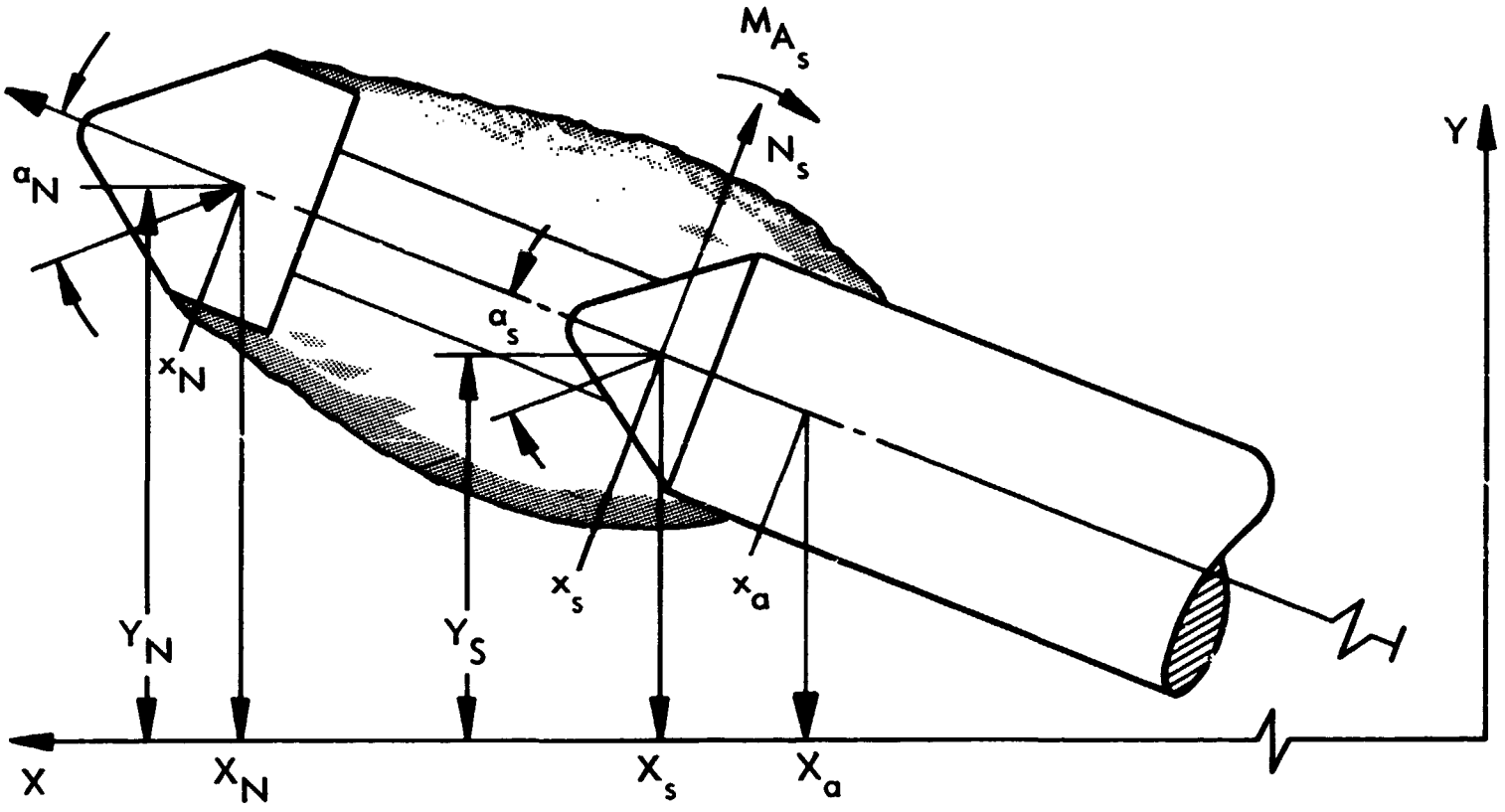

Fig. 4 Definition of Separated Flow Parameters

$$N_s(t) = \frac{\rho U^2}{2} S \left\{ \frac{\partial C_{N_s}}{\partial \alpha_s} \alpha_s(t) + \frac{\partial C_{N_s}}{\partial \alpha_N} \alpha_N(t - \Delta t) + \frac{\partial C_{N_s}}{\partial y} \left[Y_N(t - \Delta t) - Y_s(t) \right] \right\} \tag{4.2}$$

where $\Delta t = (x_N - x_s)/\bar{U}$

Δt is the time required for the force N_s to respond to changes in α_N and Y_N.

For determination of the gust penetration loads on the ascending rigid vehicle in Fig. 4, the variables α and y are simply

$$\alpha = W_g/U \quad ; \quad y(t) = (x_N - x_s)\,\alpha\,(t - \Delta t) \tag{4.3}$$

The gust velocity W_g and the vehicle velocity U are assumed to change negligibly during a time interval large enough to define the gust penetration load, e.g., the time interval required for the vehicle to travel one body length. Thus W_g is a function of the inertial space coordinate X only.

$$W_g = f\left(X - X_{g_o}\right) \tag{4.4}$$

With t_o = time of gust entry, Eq. (4.2) can then be written as follows:

$$N_s(t) = \frac{\rho U^2}{2} S \left\{ C_{N_{\alpha_L}} \frac{W_g(X_s, t - t_o)}{U} + \Delta^i C_{N_\alpha} \frac{W_g(X_N, t - \Delta t - t_o)}{U} \right\} \tag{4.5}$$

where

$$C_{N_{\alpha_L}} = \frac{\partial C_{N_s}}{\partial \alpha_s} \quad ; \quad \Delta^i C_{N_\alpha} = (x_N - x_s)\frac{\partial C_{N_s}}{\partial y} + \frac{\partial C_{N_s}}{\partial \alpha_N}$$

For the time interval with constant vehicle velocity, the gust penetration length is simply

$$X_o - X_{g_o} = (t - t_o)\,U \tag{4.6}$$

In the remainder of the report t is set equal to zero at time of gust entry, i.e.,

$$X_o - X_{g_o} = Ut \tag{4.7}$$

Thus, the gust penetration loads in the regions of separated flow on the Apollo-Saturn launch vehicle can be summed as follows:

$$N_s + M_{A_s} = \sum_{i=1}^{N_1} N_{s_i}(t) + \sum_{i=1}^{M} M_{A_{s_i}}(t)$$

$$N_{s_i}(t) = \frac{\rho U^2}{2} S \left\{ C_{N_{\alpha_L}}\left(x_{s_i}\right) \frac{W_g\left(Ut - \left[x_o - x_{s_i}\right]\right)}{U} + \Delta^i C_{N_\alpha}\left(x_{s_i}\right) \frac{W_g\left(Ut - \left[x_o - x_{s_i}\right]\kappa\right)}{U} \right\} \tag{4.8}$$

$$M_{A_{s_i}}(t) = \frac{\rho U^2}{2} Sc \left\{ C_{m_{A_{\alpha_L}}} \left(x_{s_i}\right) \frac{W_g\left(Ut - \left[x_o - x_{s_i}\right]\right)}{U} + \Delta^i C_{m_{A_\alpha}} \left(x_{s_i}\right) \frac{W_g\left(Ut - \left[x_o - x_{s_i}\right]\kappa\right)}{U} \right\}$$

$$\kappa = 1 + \left(\frac{U}{\bar{U}} - 1\right)\left(x_{N_i} - x_{s_i}\right) \Big/ \left(x_o - x_{s_i}\right) \qquad (4.8 \text{ cont})$$

In regions of attached flow, first-order momentum theory is used. It is assumed that the body is slender encugh that the axial velocity over the vehicle surface deviates negligibly from the free stream velocity. The lift per unit length of the vehicle is then the reaction to the substantial rate of change of momentum of the virtual mass per unit length (Ref. 18). The attached flow body steering effect computed in this manner agrees very well with the experimentally measured body camber effect (Ref. 23).
With the coordinate system of Figure 5, the lift can be expressed as follows:

$$\frac{dL}{dX} = -\frac{d}{dt}\left(\frac{dI}{dX}\right) = \left(U\frac{\partial}{\partial X} - \frac{\partial}{\partial t}\right)\left(\frac{dI}{dX}\right) \qquad (4.9)$$

The momentum per unit length is

$$\frac{dI}{dX} = -\rho A W = \rho A\left(\frac{dY}{dt} - W_g\right) = \rho A\left(\frac{\partial Y}{\partial t} - U\frac{\partial Y}{\partial X} - W_g\right) \qquad (4.10)$$

Thus,

$$\frac{dL}{dX} = \left(U\frac{\partial}{\partial X} - \frac{\partial}{\partial t}\right)\left[\rho A\left(-U\frac{\partial Y}{\partial X} + \frac{\partial Y}{\partial t} - W_g\right)\right]. \qquad (4.11)$$

With the gust stationary in space, $dW_g/dt = 0$ and Eq. (4.11) can be written

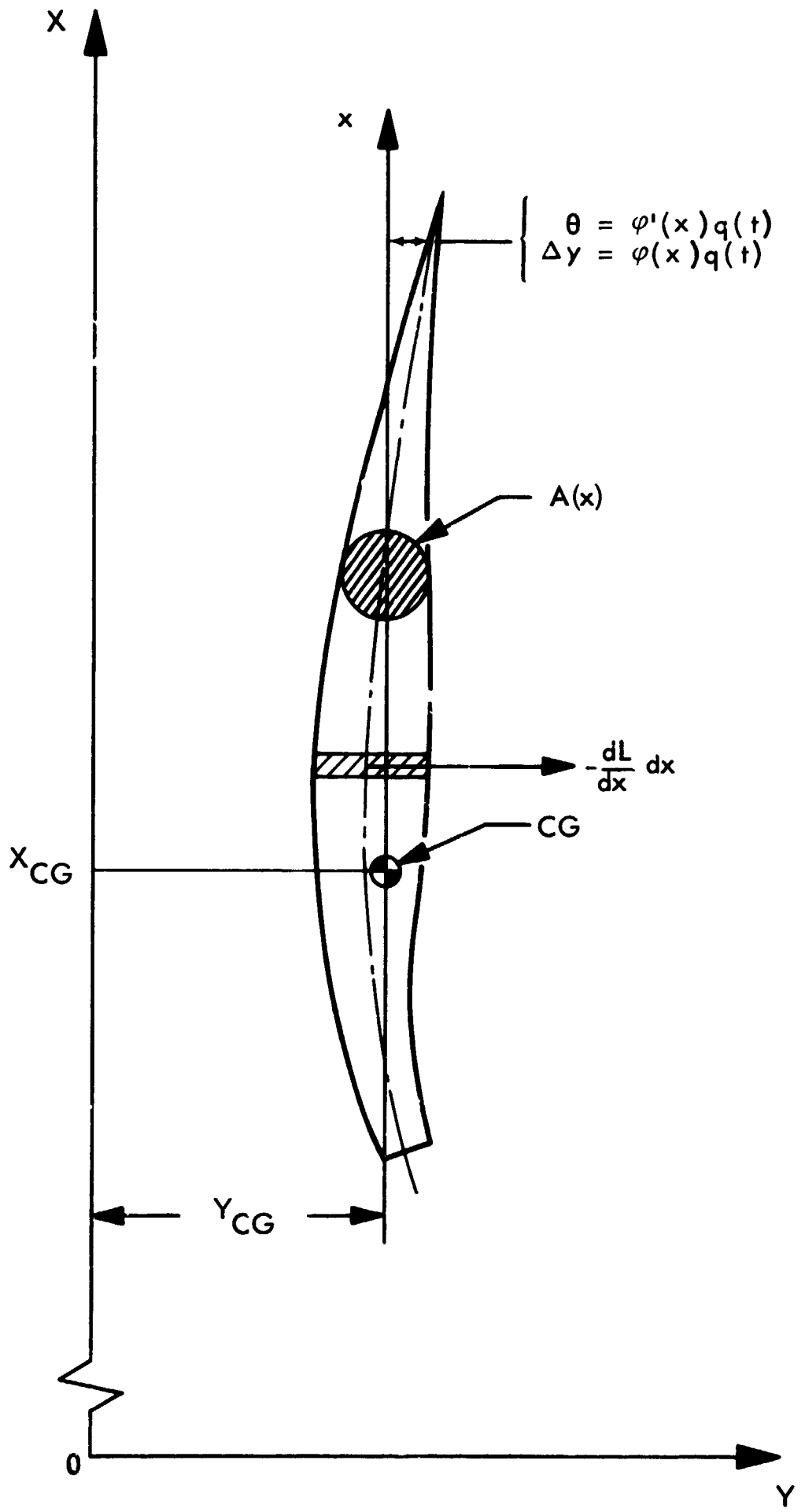

Fig. 5 Elastic Body Coordinate System

$$\frac{dL}{dX} = \left(U\frac{\partial}{\partial X} - \frac{\partial}{\partial t}\right)\left[\rho A\left(-U\frac{\partial Y}{\partial X} + \frac{\partial Y}{\partial t}\right)\right] - \left[\left(U\frac{\partial}{\partial X} - \frac{\partial}{\partial t}\right)(\rho A)\right] W_g \qquad (4.12)$$

With $L = (\rho U^2/2)SC_N$ (for the small crossflow angles considered $C_N = C_L$) Eq. (4.12) can be expressed as follows:

$$\frac{dC_N}{dX} = \left(\frac{\partial}{\partial X} - \frac{1}{U}\frac{\partial}{\partial t}\right)\left[\frac{2A}{S}\left(-\frac{\partial Y}{\partial X} + \frac{1}{U}\frac{\partial Y}{\partial t}\right)\right] - \left[\left(\frac{\partial}{\partial X} - \frac{1}{U}\frac{\partial}{\partial t}\right)\frac{2A}{S}\right]\frac{W_g}{U} \qquad (4.13)$$

For the general shape of gust profile sketched in Fig. 6, the gust velocity can be expressed as follows:

$$W_g(t) = \bar{W}_g(t) + w_g(t) \qquad (4.14)$$

where

$\bar{W}_g(t)$ = low-frequency (long wavelength) perturbation
$w_g(t)$ = high-frequency (short wavelength) perturbation

$\bar{W}_g(t)$ can be assumed to be stationary in space, and is only a function of time through the vehicle velocity U, and $w_g(t)$ represents the high-frequency, often-random type, perturbations, e.g., air turbulence. Its effect can be assessed separately, using standard statistical methods, and added to the effects of $\bar{W}_g(t)$.

In the equations [(4.3) through (4.13)] the gust considered (after gust entry) is*

$$\bar{W}_g(t - [x_o - x]/U) \qquad (4.15)$$

The gust profile $\bar{W}_g(t)$ in Fig. 6 is defined as follows

---

*The variable time and the space variable X are interchangeable in defining the gust, $X = X_{CG} + x = Ut - (x_o - x)$

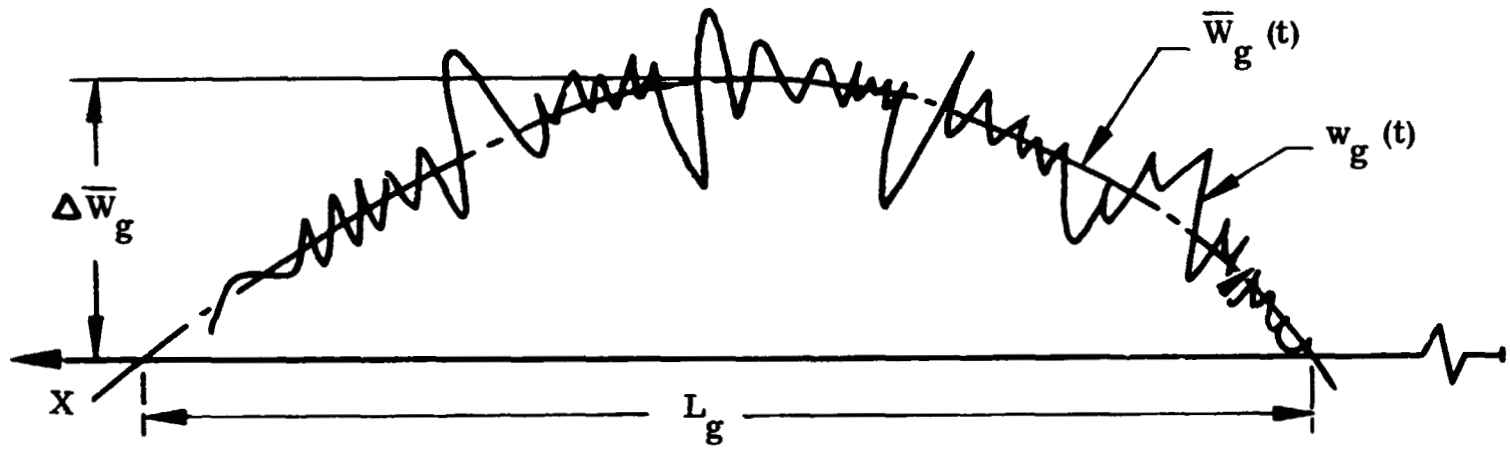

Fig. 6 General Gust Profile

$$\frac{\bar{W}_g\left(t - \frac{x_o - x}{U}\right)}{U} \Bigg/ \frac{\Delta W_g}{U} = \sin\left(\omega_g\left[t - \frac{x_o - x}{U}\right]\right) \tag{4.16}$$

where $\omega_g = 2\pi U/L_g$ = gust frequency

The gust penetration loads by themselves can often give valuable design information. However, when one wants to assess the effect on the structural integrity. one needs to go one step further, i.e., to determine the elastic vehicle response to the gust penetration loads.

4.2 ELASTIC VEHICLE RESPONSE

The equation of motion for single-degree-of-freedom bending oscillations can be written in the following form using standard notations:

$$\tilde{m}[\ddot{q}(t) + 2\zeta\omega\dot{q}(t) + \omega^2 q(t)] = P(t) \tag{4.17}$$

The generalized force P(t) is given by the virtual work done by the aerodynamic forces* on the vehicle.

$$P(t) = \int \frac{dN}{dx}\varphi(x)\,dx + \int \frac{dM_A}{dx}\varphi'(x)\,dx \tag{4.18}$$

The integrals are evaluated through summation of a discrete number of lumped forces.*

*And axial force moments.

Equation (4.2) also expresses the normal force loading in a separated flow region for the elastic vehicle, if the independent variables α and y are defined as follows (see Fig. 5):

$$\alpha = \theta - (\dot{Y}/U) + (W_g/U)$$

$$\theta = \varphi'(x)\,q(t)$$

$$Y = Y_{CG} + \varphi(x)q(t) + (x - x_{CG})\alpha(x_{CG}) \qquad (4.19)$$

The corresponding generalized force in the separated flow region can then be expressed as follows:

$$P_s(x_s,t) = [n_s(t) + N_s(t)]\varphi(x_s) + \left[m_{A_s}(t) + M_{A_s}(t)\right]\varphi'(x_s)$$

$$n_s(t) = \frac{\rho U^2}{2} S\left\{\frac{\partial C_{N_s}}{\partial \alpha_s}\left[\varphi'(x_s)q(t) - \varphi(x_s)\frac{\dot{q}(t)}{U}\right]\right.$$

$$+ \frac{\partial C_{N_s}}{\partial \theta_N}\varphi'(x_N)q(t - \Delta t) + \frac{\partial C_{N_s}}{\partial\left(\frac{\dot{Y}_N}{U}\right)}\varphi(x_N)\frac{\dot{q}(t - \Delta t)}{U}$$

$$\left. + \frac{\partial C_{N_s}}{\partial y}\left[\varphi(x_N)q(t - \Delta t) - \varphi(x_s)q(t)\right]\right\} \qquad (4.20)$$

where $m_{A_s}(t)$ is the corresponding axial force moment, $N_s(t)$ is the gust penetration load defined by Eq. (4.5), and $M_{a_s}(t)$ is its correlary for the axial force moment.

As the structural stiffness is an order of magnitude larger than the aerodynamic stiffness, the effect of aerodynamic forces on the bending frequency is negligibly small. The structural and aerodynamic damping are two orders of magnitude less

than critical. Consequently, the vehicle may be assumed to describe harmonic oscillations with the natural free-free bending frequency, and $q(t - \Delta t)$ can be expressed as follows:

$$q(t - \Delta t) = e^{-i\omega \Delta t} q(t) = \cos(\omega \Delta t)\, q(t) - \sin(\omega \Delta t)[iq(t)] \qquad (4.21)$$

where $\dot{q}(t) = \omega[iq(t)]$.*

In regions of attached flow, first-order momentum theory is used. Equation (4.11) together with Eq. (4.19) gives

$$\frac{dL}{dx} = -\rho U^2 \left(\frac{\partial}{\partial x} \left\{ A(x) \left[\varphi'(x) q(t) - \varphi(x) \frac{\dot{q}(t)}{U} \right] \right\} - A(x) \left[\varphi'(x) \frac{\dot{q}(t)}{U} - \varphi(x) \frac{\ddot{q}(t)}{U^2} \right] \right) - A'(x) \frac{W_g}{U} \qquad (4.22)$$

With $L = (\rho U^2/2) S C_N$, Eq. (4.30) can be written in coefficient form as follows:

$$\frac{dC_N}{dx} = -\frac{\partial}{\partial x} \left(\frac{2A(x)}{S} \left[\varphi'(x) q(t) - \varphi(x) \frac{\dot{q}(t)}{U} \right] \right) + \frac{2A(x)}{S} \left[\varphi'(x) \frac{\dot{q}(t)}{U} - \varphi(x) \frac{\ddot{q}(t)}{U^2} \right] - \frac{2A'(x)}{S} \frac{W_g}{U} \qquad (4.23)$$

Equations (4.18) and (4.23) together describe the following generalized force. (The axial force moment is zero for the slender body assumed in the first order momentum theory.)

$$P_a(t) = \int_{x_i}^{x_{i+1}} \frac{dL}{dx} \varphi(x)\, dx = \frac{\rho U^2}{2} S \int_{x_i}^{x_{i+1}} \frac{dC_N}{dx} \varphi(x)\, dx \qquad (4.24)$$

*This makes $2\zeta\omega\dot{q}(t)$ in Eq. (4.17) equivalent to the often used notation $i g \omega^2 q(t)$, where $g = 2\zeta$.

With dC_N/dx defined by Eq. (4.23), integrating by parts gives

$$\int_{x_i}^{x_{i+1}} \frac{dC_N}{dx}\,\varphi(x)\,dx$$

$$= -\int_{x_i}^{x_{i+1}} \frac{2A(x)}{S}\,\varphi(x)\left[\varphi'(x)q(t) - \varphi(x)\,\frac{\dot{q}(t)}{U}\right] + \int_{x_i}^{x_{i+1}} \frac{2A(x)}{S}\left\{[\varphi'(x)]^2 q(t) - [\varphi(x)]^2\,\frac{\ddot{q}(t)}{U^2}\right\} dx$$

$$- \int_{x_i}^{x_{i+1}} \frac{2A'(x)}{S}\,\varphi(x)\,\frac{W_g(X_{CG} + x)}{U}\,dx \qquad (4.25)$$

For the long wavelength gusts and lower bending modes considered in the present analysis, the area change $A'(x)$ at interstage frustums and on the command module of the Apollo-Saturn launch vehicle takes place over an x-extent that is small compared to gust and bending mode "wavelengths." Thus, in the evaluation of the integrals in Eq. (4.25) the x-step can be increased appreciably if the fast area change $A'(x)$ is "integrated out" [considering $\varphi(x)$, $\varphi'(x)$, and $W_g(X_{CG} + x)$ constant over the x-interval between x_i and x_{i+1}]. Thus, Eq. (4.25) is rewritten in the following form for the Apollo-Saturn type geometry, i.e., for conical area changing sections.

$$\int_{x_i}^{x_{i+1}} \frac{dC_N}{dx}\,\varphi(x)\,dx$$

$$= -\left[\frac{2A(x_{i+1})}{S}\,\varphi(x_{i+1})\varphi'(x_{i+1}) - \frac{2A(x_i)}{S}\,\varphi(x_i)\varphi'(x_i)\right]q(t) + \left\{\frac{2A(x_{i+1})}{S}\,[\varphi(x_{i+1})]^2\right.$$

$$\left. - \frac{2A(x_i)}{S}\,[\varphi(x_i)]^2\right\}\frac{\dot{q}(t)}{U} + \frac{2\pi}{3S}(x_{i+1} - x_i)\,\frac{[r(x_{i+1})]^3 - [r(x_i)]^3}{r(x_{i+1}) - r(x_i)}\left\{[\varphi'(\bar{x}_i)]^2 q(t)\right.$$

$$\left. - [\varphi(\bar{x}_i)]^2\,\frac{\ddot{q}(t)}{U^2}\right\} - \left[\frac{2A(x_{i+1})}{S} - \frac{2A(x_i)}{S}\right]\varphi(\bar{x}_i)\,\frac{W_g(X_{CG} + \bar{x}_i)}{U} \qquad (4.26\text{-}1)$$

For constant area sections the gust shear $W'_g(X)$ and the modal slope $\varphi'(x)$ can be assumed to remain constant for the (small) x-interval $x_i \leq x \leq x_{i+1}$ resulting in the following expression for Eq. (4.25)

$$\int_{x_i}^{x_{i+1}} \frac{dC_N}{dx} \varphi(x)\, dx =$$

$$-\frac{2A(x_{i+1})}{S}\left[\left[\varphi(x_{i+1})\varphi'(x_{i+1}) - \varphi(x_i)\varphi'(x_i)\right]q(t) - \left(\left[\varphi(x_{i+1})\right]^2 - \left[\varphi(x_i)\right]^2\right)\frac{\dot{q}(t)}{U}\right.$$

$$\left.\frac{(x_{i+1} - x_i)}{6}\left(\varphi[(x_{i+1})]^2 - [\varphi(x_i)]^2\right)\frac{\ddot{q}(t)}{U^2}\right] \qquad (4.26\text{-}2)$$

The $\ddot{q}$-terms in Eq. (4.26) can be neglected as the aerodynamic inertia is negligibly small compared to the structural (and rigid body) inertia.

In regions of separated flow, the lumped generalized force is defined as follows (through Eqs. (4.2), (4.18), and (4.19).

$$P_s(x_s, t) = N_s(t)\ \phi(x_s) + M_{A_s}(t)\ \phi'(x_s)$$

$$N_s(t) \Big/ \left(\frac{\rho U^2}{2}\right) S = \frac{\partial C_{N_s}}{\partial \alpha_s}\left[\phi'(x_s)q(t)\right.$$

$$- \phi(x_s)\ \frac{\dot{q}(t)}{U}\Bigg] + \frac{\partial C_{N_s}}{\partial \theta_N}\,\phi'(x_N)q(t-\Delta t) + \frac{\partial C_{N_s}}{\partial\left(\frac{\dot{Y}_N}{U}\right)}\,\phi(x_N)\,\frac{\dot{q}(t-\Delta t)}{U} + \frac{\partial C_{N_s}}{\partial y}\Big[\phi(x_N)q(t-\Delta t)$$

$$- \phi(x_s)q(t)\Big] + \frac{\partial C_{N_s}}{\partial \alpha_s}\,\frac{W_g\left(Ut - \left[x_o - x_s\right]\right)}{U}$$

$$+ \left[(x_N - x_s)\ \frac{\partial C_{N_s}}{\partial y} + \frac{\partial C_{N_s}}{\partial \alpha_N}\right]\ \frac{W_g\left(Ut - \left[x_o - x_s\right]\kappa\right)}{U}$$

$$\kappa = 1 + \left(\frac{U}{\bar{U}} - 1\right)\left(x_{N_i} - x_{s_i}\right)\Big/\left(x_o - x_{s_i}\right) \tag{4.27}$$

$M_{A_s}(t)\Big/\left(\frac{\rho U^2}{2}\right)Sc$ is the axial force moment term corresponding to N_s (t) (given by the same equation with C_{m_A} substituted for C_N). In comparing Eq. (4.27) with Eq. (4.25), one notes that the separated flow region is treated as a dead air region; that is, no body steering effects are considered. It was shown in Ref. 4 that if one included some steering effect by equating the local lift generation to that of an equivalent attached flow region with reduced cross sectional area, improved predictions of the unsteady aerodynamics resulted.

The effective cross sectional area in separated flow regions is determined by the average reduction in dynamic pressure, which for a flared section is given by the axial force deficit.

$$\bar{A}(x_i)/A(x_i) = \bar{\rho}\bar{U}^2/\rho U^2 = \left(C_{A_F}\right)_s\Big/\left(C_{A_F}\right)_a \tag{4.28}$$

If we assume that the density changes negligibly throughout the separated flow region, which should be permissible at the subsonic and transonic vehicle speeds of interest, the effective area is related to the mean convection velocity $\bar{U}$ as follows:

$$\bar{A}(x_i)/A(x_i) = \left[\bar{U}(x_i)/U(x_i)\right]^2 \tag{4.29}$$

Applying this equivalent area rule gives the following expression for the generalized forces, combining Eqs. (4.25), (4.27), and (4.29).

$$P(t) = \sum_{i=1}^{N} P_{N_i}(t) + P_{N_{Fins}}(t) + \sum_{i=1}^{M} P_{M_i}(t)$$

$$P_{N_i}(t) \Big/ \left(\frac{\rho U^2}{2}\right) S = \left\{ C_{N_{\alpha_L}} \phi(x_{i_L}) \phi'(x_{i_L}) + \left(\frac{\bar{U}}{U}\right)^2 \frac{2A(x_{i+1})}{S} [\phi(x_i)\phi'(x_i) - \phi(x_{i+1})\phi'(x_{i+1})] \right\} q(t)$$

$$- \left(C_{N_{\alpha_L}} [\phi(x_{i_L})]^2 - \left(\frac{\bar{U}}{U}\right)^2 \frac{2A(x_{i+1})}{S} \left\{ [\phi(x_i)]^2 - [\phi(x_{i+1})]^2 \right\} \right) \frac{\dot{q}(t)}{U}$$

$$+ \frac{2\pi}{S} \left(\frac{\bar{U}}{U}\right)^2 \frac{(x_{i+1} - x_i)}{3} \left[\frac{[r(x_{i+1})]^3 - [r(x_i)]^3}{r(x_{i+1}) - r(x_i)} \right]^*$$

$$[\phi'(\bar{x}_i)]^2 q(t) + C_{N_{\alpha_L}} \phi(x_{i_L}) \frac{W_g(Ut - [x_o - x_{i_L}])}{U}$$

$$+ \left(\frac{\bar{U}}{U}\right)^2 \left(\frac{2A(x_{i+1})}{S} - \frac{2A(x_i)}{S} \right) \phi(\bar{x}_i) \frac{W_g(Ut - [x_o - \bar{x}_i])}{U} \qquad (4.30 \text{ start})$$

*Equal to zero for constant area sections.

$$+ \frac{\partial\left[C_{N_s}(\bar{x}_i)\right]}{\partial\left[\theta\left(x_{N_i}\right)\right]} \phi(\bar{x}_i)\,\phi'\left(x_{N_i}\right)\, q(t-\Delta t)$$

$$+ \frac{\partial\left[C_{N_s}(\bar{x}_i)\right]}{\partial\left[\dfrac{\dot{Y}\left(x_{N_i}\right)}{U}\right]} \phi(\bar{x}_i)\,\phi\left(x_{N_i}\right)\frac{\dot{q}(t-\Delta t)}{U}$$

$$+ \frac{\partial\left[C_{N_s}(\bar{x}_i)\right]}{\partial\beta} \frac{\phi(\bar{x}_i)\,\phi\left(x_{N_i}\right)}{\left(x_{N_i}-\bar{x}_i\right)}\, q(t-\Delta t)$$

$$- \frac{\partial\left[C_{N_s}(\bar{x}_i)\right]}{\partial\beta} \frac{\left[\phi(\bar{x}_i)\right]^2}{\left(x_{N_i}-\bar{x}_i\right)}\, q(t) + \left\{\frac{\partial\left[C_{N_s}(\bar{x}_i)\right]}{\partial\left[\theta\left(x_{N_i}\right)\right]}\right.$$

$$\left. + \frac{\partial\left[C_{N_s}(\bar{x}_i)\right]}{\partial\beta}\right\} \phi(\bar{x}_i)\,\frac{W_g\left(Ut-\left[x_o-\bar{x}_i\right]\kappa\right)}{U} \qquad (4.30 \text{ cont})$$

$$P_{N_{Fins}}(t) \Big/ \left(\frac{\rho U^2}{2}\right) S = C_{N_{\alpha_{Fins}}} \left\{ \phi(x_{TE})\phi'(x_{TE})q(t) \right.$$

$$\left. - [\phi(x_{TE})]^2 \frac{\dot{q}(t)}{U} + \phi(x_{TE}) \frac{W_g(Ut - [x_o - x_{TE}])}{U} \right\}^*$$

$$P_{M_i}(t) \Big/ \left(\frac{\rho U^2}{2}\right) Sc = C_{m_{A_{\alpha_L}}} [\phi'(\bar{x}_i)]^2 q(t) - C_{m_{A_{\alpha_L}}} \phi(\bar{x}_i)\phi'(\bar{x}_i) \frac{\dot{q}(t)}{U}$$

$$+ \frac{\partial \left[C_{m_{A_s}}(\bar{x}_i)\right]}{\partial \left[\theta\left(x_{N_i}\right)\right]} \phi'(\bar{x}_i)\phi'\left(x_{N_i}\right) q(t - \Delta t)$$

$$+ \frac{\partial \left[C_{m_{A_s}}(\bar{x}_i)\right]}{\partial \left[\dot{Y}\left(x_{N_i}\right)/U\right]} \phi'(\bar{x}_i)\phi\left(x_{N_i}\right) \frac{\dot{q}(t - \Delta t)}{U}$$

$$+ \frac{\partial \left[C_{m_{A_s}}(\bar{x}_i)\right]}{\partial \beta} \frac{\phi'(\bar{x}_i)\phi\left(x_{N_i}\right)}{\left(x_{N_i} - \bar{x}_i\right)} q(t - \Delta t) \qquad \text{(4.30 cont)}$$

*The body portion "inside" the fins is treated as part of $\sum_{i=1}^{N} P_{N_i}(t)$.

$$- \frac{\partial\left[C_{m_{A_s}}(\bar{x}_i)\right]}{\partial\beta} \frac{\phi'(\bar{x}_i)\phi(\bar{x}_i)}{\left(x_{N_i} - \bar{x}_i\right)} q(t) + \left\{ \frac{\partial\left[C_{m_{A_s}}(\bar{x}_{i)}\right]}{\partial\left[e\left(x_{N_i}\right)\right]} \right.$$

$$\left. + \frac{\partial\left[C_{m_{A_s}}(\bar{x}_{i'}\right]}{\partial\beta} \right\} \phi'(\bar{x}_i) \frac{W_g(Ut - [x_o - x_i]\kappa)}{U}$$

(4.30 concluded)

$C_{N_{\alpha_L}}$ is the local force derivative, i.e., $C_{N_{\alpha_L}} = \frac{\partial C_{N_s}}{\partial \alpha_s}$ at $x_{i_L} = \bar{x}_i$ in separated flow regions and equal to the total normal force derivative over an area changing section ending at $x_{i_L} = x_i$ in attached flow regions.

($C_{m_{A_{\alpha_L}}}$ is always the separated flow derivative $\frac{\partial C_{m_A)}}{\partial \alpha_s}$

Using Eq. (4.21), simplified for the slow frequencies of practical interest in the present quasi-steady analysis, i.e., with $\cos \omega\Delta t = 1$ and $\sin \omega\Delta t = \omega\Delta t$, gives Eq. (4.30) in the following form:

$$P(t) = \frac{\rho U^2}{2} S \left\{ \left(\sum_{i=1}^{N} K_i + K_{Fins} \right) q(t) \right.$$

$$\left. + \left(\sum_{i=1}^{N} D_i + D_{Fins} \right) \frac{\dot{q}(t)}{U} + \sum_{i=1}^{N} G_i(t) + G_{Fins}(t) \right\} \qquad (4.31 \text{ start}).$$

$$K_i = C_{N_{\alpha_L}} \phi(x_{i_L}) \phi'(x_{i_L}) + cC_{m_{A_{\alpha_L}}} [\phi'(\bar{x}_i)]^2$$

$$+ \left(\frac{\bar{U}}{U}\right)^2 \frac{2A(x_{i+1})}{S} [\phi(x_i)\phi'(x_i) - \phi(x_{i+1})\phi'(x_{i+1})]$$

$$+ \frac{2\pi}{S} \left(\frac{\bar{U}}{U}\right)^2 \left(\frac{x_{i+1} - x_i}{3}\right) \left(\frac{[r(x_{i+1})]^3 - [r(x_i)]^3}{r(x_{i+1}) - r(x_i)}\right)^* [\phi'(\bar{x}_i)]^2$$

$$+ \left\{ \frac{\partial \left[C_{N_s}(\bar{x}_i)\right]}{\partial \left[\theta\left(x_{N_i}\right)\right]} \phi(\bar{x}_i) + \frac{\partial \left[C_{m_{A_s}}(\bar{x}_i)\right]}{\partial \left[\theta\left(x_{N_i}\right)\right]} c\phi'(x_i) \right\} \phi'\left(x_{N_i}\right)$$

$$+ \left\{ \frac{\partial \left[C_{N_s}(\bar{x}_i)\right]}{\partial \beta} \phi(\bar{x}_i) + \frac{\partial \left[C_{M_{A_s}}(\bar{x}_i)\right]}{\partial \beta} c\phi'(\bar{x}_i) \right\}$$

$$\frac{\phi\left(x_{N_i}\right) - \phi(\bar{x}_i)}{\left(x_{N_i} - \bar{x}_i\right)}$$

$$K_{Fins} = C_{N_{\alpha_{Fins}}} \phi(x_{TE}) \phi'(x_{TE}) \qquad \text{(4.31 cont)}$$

*Equal to zero for constant area sections.

$$D_i = -C_{N_{\alpha_L}} [\phi(x_{i_L})]^2 - cC_{m_{A_{\alpha_s}}} \phi(\bar{x}_i)\phi'(\bar{x}_i)$$

$$\cdot \left(\frac{\bar{U}}{U}\right)^2 \frac{2A(x_{i+1})}{S} \left\{[\phi(x_i)]^2 - [\phi(x_{i+1})]^2\right\}$$

$$\left\{\frac{\partial\left[C_{N_s}(\bar{x}_i)\right]}{\partial\left[\theta\left(x_{N_i}\right)\right]}\phi(\bar{x}_i) + \frac{\partial\left[C_{m_{A_s}}(\bar{x}_i)\right]}{\partial\left[\theta\left(x_{N_i}\right)\right]} c\phi'(\bar{x}_i)\right\} \phi'\left(x_{N_i}\right) U\Delta t_i$$

$$-\left\{\frac{\partial\left[C_{N_s}(\bar{x}_i)\right]}{\partial\left[\dot{Y}\left(x_{N_i}\right)/U\right]}\phi(\bar{x}_i) + \frac{\partial\left[C_{m_{A_s}}(\bar{x}_i)\right]}{\partial\left[\dot{Y}\left(x_{N_i}\right)/U\right]} c\phi'(\bar{x}_i)\right\}\phi\left(x_{N_i}\right)$$

$$-\left\{\frac{\partial\left[C_{N_s}(\bar{x}_i)\right]}{\partial\beta}\phi(\bar{x}_i) + \frac{\partial\left[C_{m_{A_s}}(\bar{x}_i)\right]}{\partial\beta} c\phi'(\bar{x}_i)\right\} \frac{\phi\left(x_{N_i}\right) U\Delta t_i}{\left(x_{N_i} - \bar{x}_i\right)}$$

$$D_{Fins} = -C_{N_{\alpha_{Fins}}} [\phi(x_{TE})]^2 \qquad \text{(4.31 cont)}$$

$$G_i(t) = C_{N_{\alpha_L}} \phi(x_{i_L}) \frac{W_g(Ut - [x_o - x_{i_L}])}{U}$$

$$+ cC_{m_{A_{\alpha_s}}} \phi'(\bar{x}_i) \frac{W_g(Ut - [x_o - \bar{x}_i])}{U}$$

$$+ \left(\frac{\bar{U}}{U}\right)^2 \left[\frac{2A(x_{i+1})}{S} - \frac{2A(x_i)}{S}\right] \phi(\bar{x}_i) \frac{W_g(Ut - [x_o - \bar{x}_i])}{U}$$

$$+ \left\{\frac{\partial\left[C_{N_s}(\bar{x}_i)\right]}{\partial\left[\theta\left(x_{N_i}\right)\right]} + \frac{\partial\left[C_{N_s}(\bar{x}_i)\right]}{\partial\beta}\right\} \phi(\bar{x}_i) \frac{W_g(Ut - [x_o - \bar{x}_i]\kappa}{U}$$

$$+ \left\{\frac{\partial\left[C_{m_{A_s}}(\bar{x}_i)\right]}{\partial\left[\theta\left(x_{N_i}\right)\right]} + \frac{\partial\left[C_{m_{A_s}}(\bar{x}_i)\right]}{\partial\beta}\right\} c\phi'(x_i) \frac{W_g(Ut - [x_o - \bar{x}_i]\kappa)}{U}$$

$$G_{Fins}(t) = C_{N_{\alpha_{Fins}}} \phi(x_{TE}) \frac{W_g(Ut - [x_o - x_{TE}])}{U}$$

(4.31 concluded)

The time-lag effect is usually obtained as follows:

$$U^{**} = \left(x_{N_i} - \bar{x}_i\right) \Big/ \left(\frac{\bar{U}}{U}\right) \tag{4.32}$$

In regions of shock-induced separation upstream of interstage flares, x_{N_i} is substituted by x_{AC}, the aerodynamic center for the loads on the body upstream of the separation. This is true for the separation-induced negative cylinder load. For the positive load induced on the flare, an additional time lag through the separated flow region is realized. A detailed description of these deviations is given in Refs. 12 and 20.

It has been demonstrated that, in addition to the downstream convection effect on bodies submerged in wakes, upstream communication effects will in some cases become important (Refs. 2, 5, and 24). That is, the change of the submerged body force by an amount ΔC_{N_s} causes a wake translation $\Delta y = (\partial y/\partial C_{N_s})\Delta C_{N_s}$. The force change due to this "wake flipping" Δy is associated with an upstream-downstream time lag

$$\Delta t_u + \Delta t = \left(x_{N_i} - \bar{x}_i\right) \Big/ \bar{U}_u + \left(x_{N_i} - \bar{x}_i\right) \Big/ \bar{U}$$

The modification needed to include these upstream communication effects in the computation has been described in Ref. 20. The results of a recently completed study (Ref. 5) indicate that the upstream communication effects are negligible except for certain critical geometries.

By combining Eqs. (4.26) and (4.27) the equation of motion for single-degree-of-freedom bending oscillations can be written in the following form

$$\ddot{q}(t) + 2\omega\left[\zeta - \frac{B}{2\omega U}\left(\sum_{i=1}^{N} D_i + D_{Fins}\right)\right]\dot{q}(t) + \omega^2\left[1 - \frac{B}{\omega^2}\left(\sum_{i=1}^{N} K_i + K_{Fins}\right)\right]q(t)$$

$$= B\left[\sum_{i=1}^{N} G_i(t) + G_{Fins}(t)\right] \qquad (4.33)$$

where $B = (\rho U^2/2)S/\tilde{m}$.

Since the aerodynamic stiffness is negligible compared to the structural stiffness, i.e.,

$$\left|\frac{B}{\omega^2}\left(\sum_{i=1}^{N} K_i + K_{Fins}\right)\right| << 1$$

Eq. (4.33) can be approximated as

$$\ddot{q}(t) + 2\omega\zeta_T\dot{q}(t) + \omega^2 q(t) = g(t)$$

$$\zeta_T = \zeta - \frac{B}{2\omega U}\left(\sum_{i=1}^{N} D_i + D_{Fins}\right)$$

$$g(t) = B\left[\sum_{i=1}^{N} G_i(t) + G_{Fins}(t)\right] \qquad (4.34)$$

where $\left(\sum_{i=1}^{N} D_i + D_{Fins}\right)$ is given by Eq. (4.31)

The gust function g(t) is defined through Eq. (4.31) as follows (using time rather than the space coordinate X as independent variable):

$$g(t) = \sum_{i=1}^{N_1} C_{1_i} \frac{W_g(t - [x_o - x_i]/U)}{U} + \sum_{i=1}^{N_2} C_{2_i} \frac{W_g(t - [x_o - \bar{x}_i]/U)}{U}$$

$$+ \sum_{i=1}^{N_3} C_{3_i} \frac{W_g(t - [x_o - \bar{x}_i]\,\kappa/U)}{U} + BC_{N_{\alpha_{Fins}}} \phi(x_{TE}) \frac{W_g(t - [x_o - x_{TE}]/U)}{U}$$

$$C_{1_i} = BC_{N_{\alpha_L}} \phi(x_i)$$

$$C_{2_i} = B\left\{C_{N_{\alpha_s}} \phi(\bar{x}_i) + cC_{m_{A_{\alpha_s}}} \phi'(\bar{x}_i) + \left(\frac{\bar{U}}{U}\right)^2 \left[\frac{2A(x_{i+i})}{S} - \frac{2A(x_i)}{S}\right]\right\}$$

$$C_{3_i} = B\left\{\frac{\partial\left[C_{N_s}(\bar{x}_i)\right]}{\partial\left[\theta\left(x_{N_i}\right)\right]} + \frac{\partial\left[C_{N_s}(\bar{x}_i)\right]}{\partial\beta}\right\} \phi(\bar{x}_i)$$

$$+ B\left\{\frac{\partial\left[C_{m_{A_s}}(\bar{x}_i)\right]}{\partial\left[\theta\left(x_{N_i}\right)\right]} + \frac{\partial\left[C_{m_{A_s}}(\bar{x}_i)\right]}{\partial\beta}\right\} c\,\phi'(\bar{x}_i) \qquad (4.35)$$

The sinusoidal gust is defined as follows

$$\frac{\overline{W}_g\left(t - \frac{x_o - x}{U}\right)}{U} \Bigg/ \frac{\Delta W_g}{U} = \sin\left(\omega_g\left[t - \frac{x_o - x}{U}\right]\right) \tag{4.36}$$

Using Laplace transformation, i.e.,

$$\hat{q}(s) = \int_0^\infty e^{-st}\, q(t)\, dt$$

Eq. (4.35) can be written in the frequency domain in the following form (see, for example, Ref. 25):

$$\begin{aligned} \hat{q}(s) &= \hat{q}_o(s) + \hat{q}_g(s) \\ \hat{q}_o(s) &= \left[\dot{q}(0) + (s + 2\omega\zeta_T)q(0)\right] / D(s) \\ \hat{q}_g(s) &= \hat{\bar{q}}(s)/D(s) \\ D(s) &= s^2 + 2\omega\zeta_T s + \omega^2 \end{aligned} \tag{4.37}$$

$q(0)$ and $\dot{q}(0)$ are the normalized bending mode deflection and deflection rate at gust entry, respectively. The Laplace transform of Eq. (4.35) gives the following definition of $\hat{\bar{g}}(s)$:

$$\hat{\bar{g}}(s) = \frac{\hat{\bar{W}}_g(s)}{U}\left\{\sum_{i=1}^{N_1} C_{1_i} \exp\left[-\left(\frac{x_o - x_i}{U}\right)s\right] + \sum_{i=1}^{N_2} C_{2_i} \exp\left[-\left(\frac{x_o - \bar{x}_i}{U}\right)s\right]\right.$$

$$+ \sum_{i=1}^{N_3} C_{3_i} \exp\left[-\left(\frac{x_o - \bar{x}_i)\kappa}{U}\right)s\right] + BC_{N_\alpha}{}_{Fins} \phi(x_{TE}) \exp\left[-\left(\frac{x_o - x_{TE}}{U}\right)s\right] \Bigg\}$$

Eq. (4.36) gives the following $\hat{\bar{W}}_g(s)$ (4.38)

$$\frac{\hat{\bar{W}}_g(s)}{U} \Big/ \frac{\Delta W_g}{U} = \omega_g / \left(s^2 + \omega_g^2\right) \tag{4.39}$$

Defining a new function $\hat{\bar{f}}(s)$ as follows

$$\hat{\bar{f}}(s) = \frac{\hat{\bar{W}}_g(s)}{U} \Big/ D(s) \tag{4.40}$$

gives the following expression for $\hat{q}_{\bar{g}}(s)$ in Eq. (4.37)

$$\hat{q}_{\bar{g}}(s) = \hat{\bar{f}}(s) \Bigg(\sum_{i=1}^{N_1} C_{1_i} \exp\left[-\left(\frac{x_o - x_i}{U}\right)s\right] + \sum_{i=1}^{N_2} C_{2_i} \exp\left[-\left(\frac{x_o - \bar{x}_i}{U}\right)s\right] + \sum_{i=1}^{N_3} C_{3_i} \exp\left\{-\left[\frac{(x_o - x_i)\kappa}{U}\right]s\right\} + BC_{N_\alpha}{}_{Fins} \varphi(x_{TE}) \exp\left[-\left(\frac{x_o - x_{TE}}{U}\right)s\right] \Bigg) \tag{4.41}$$

The corresponding formulation in the time domain can be written (Ref. 25)

$$q_{\bar{g}}(t) = \sum_{i=1}^{N_1} C_{1_i} \bar{f}\left(t - \frac{x_o - x_i}{U}\right) + \sum_{i=1}^{N_2} C_{2_i} \bar{f}\left(t - \frac{x_o - x_{i+1}}{U}\right) + \sum_{i=1}^{N_3} C_{3_i} \bar{f}\left(t - \frac{x_o - \bar{x}_i}{U}\right)$$

$$+ \sum_{i=1}^{N_4} C_{4_i} \bar{f}\left[t - \frac{(x_o - \bar{x}_i)\kappa}{U}\right] + BC_{N_\alpha}{}_{Fins} \varphi(x_{TE}) \bar{f}\left(t - \frac{x_o - x_{TE}}{U}\right) \qquad (4.42)$$

For the gust profiles given by Eq. (4.36), the following expressions are obtained for $\hat{f}(s)$ and $\bar{f}(t)$ (Ref. 25).

$$\hat{\bar{f}}(s) \Big/ \frac{\Delta W_g}{U} = \omega_g \Big/ \left(s^2 + \omega_g^2\right) D(s) \qquad (4.43)$$

$$\bar{f}(t) = \frac{\Delta W_g}{U} \frac{\sin(\omega_g t - \psi_1) + \dfrac{\exp(-\omega\zeta_T t)}{(\omega/\omega_g)\left(1 - \zeta_T^2\right)^{1/2}} \sin\left\{\omega t\left[1 - \zeta_T^2\right]^{1/2} - \psi_2\right\}}{\omega_g^2\left\{\left[(\omega/\omega_g)^2 - 1\right]^2 + 4(\omega/\omega_g)^2\zeta_T^2\right\}^{1/2}}$$

$$\tan\psi_1 = \frac{2(\omega/\omega_g)\zeta_T}{(\omega/\omega_g)^2 - 1} \quad ; \quad \tan\psi_2 = \frac{2(\omega/\omega_g)^2\zeta_T\left(1-\zeta_T^2\right)^{1/2}}{(\omega/\omega_g)^2\left(1 - 2\zeta_T^2\right) - 1} \qquad (4.44)$$

As $\zeta_T^2 << 1$ Eq. (4.44) can be simplified as follows:

$$\bar{f}(t) = \frac{\Delta W_g}{U} \frac{\sin(\omega_g t - \psi_1) + (\omega_g/\omega)\exp(-\omega\zeta_T t)\sin(\omega t - \psi_2)}{\omega^2\left\{\left[1 - (\omega_g/\omega)^2\right]^2 + 4(\omega_g/\omega)^2\zeta_T^2\right\}^{1/2}}$$

$$\tan\psi_1 = \frac{2(\omega_g/\omega)\zeta_T}{1 - (\omega_g/\omega)^2} \quad ; \quad \tan\psi_2 = \frac{2\zeta_T}{1 - (\omega_g/\omega)^2} \qquad (4.45)$$

or

$$\bar{f}(t) = \frac{\Delta W_g}{U} \frac{1}{\omega^2} \frac{1}{2\zeta_T} \frac{1 + \exp(-\omega\zeta_T t)}{\left[1 + (\epsilon/\zeta_T)^2\right]^{1/2}} \cos\left(\omega t + \arctan\frac{\epsilon}{\zeta_T}\right) \qquad (4.46)$$

where

$$\omega/\omega_g = 1 + \epsilon$$
$$|\epsilon| \ll 1$$
$$\zeta_T \neq 0$$

The effect of the initial conditions at gust entry are obtained as follows (Ref. 25):

$$\hat{q}_o(s) = \frac{\dot{q}(0) + (s + 2\omega\zeta_T)q(0)}{(s + \omega\zeta_T)^2 + \omega^2\left(1 - \zeta_T^2\right)} \qquad (4.47)$$

$$q_o(t) = q(0)\sqrt{1 + [2\zeta_T + \dot{q}(0)/\omega q(0)]^2}\; e^{-\omega\zeta_T t} \cos\{\omega t - \arctan[\zeta_T + \dot{q}(0)/\omega q(0)]\} \qquad (4.48)$$

Or with $t = t' + t_o$

$$q_o(t') = \Delta q_o\, e^{-\omega\zeta_T t} \cos(\omega t' + \psi_o)$$

$$\Delta q_o = q(0)\sqrt{1 + [2\zeta_T + \dot{q}(0)/\omega q(0)]^2}\; \exp\left(-\omega\zeta_T \Delta t_o\right)$$

$$\psi_o = \omega\,\Delta t_o - \arctan[\zeta_T + \dot{q}(0)/\omega q(0)] \qquad (4.49)$$

That is, the initial conditions can be expressed by the amplitude Δq_0 and phase angle ψ_0 at gust entry. For the linear analysis performed here, the effects of these oscillatory parameters at gust entry on the overall bending response can be superimposed on the gust response.

Combining Eq. (4.42) with Eqs. (4.45), and (4.46) gives the following definition of the bending response to sinusoidal type gusts.

For algebraic shorthand purposes, Eq. (4.42) is represented by the following formulation:

$$q_{\bar{g}}(t) = \sum_{n=1}^{N} C_n \bar{f}(t - \Delta t_n) \qquad (4.42a)$$

$\omega_g \neq \omega$

$$q_{\bar{g}}(t) = \sqrt{E_1^2 + E_2^2}\, \sin\left(\omega_g t - \arctan\frac{E_2}{E_1}\right) + e^{-\omega\zeta_T t}\sqrt{E_3^2 + E_4^2}\, \sin\left(\omega t - \arctan\frac{E_4}{E_3}\right)$$

$$E_1 = \frac{\Delta W_g}{U} \frac{1}{\omega^2\left\{\left[1 - (\omega_g/\omega)^2\right]^2 + 4(\omega_g/\omega)^2\zeta_T^2\right\}^{1/2}} \sum_{n=1}^{N} C_n \cos(\psi_1 + \omega_g \Delta t_n)$$

$$E_2 = \frac{\Delta W_g}{U} \frac{1}{\omega^2\left\{\left[1 - (\omega_g/\omega)^2\right]^2 + 4(\omega_g/\omega)^2\zeta_T^2\right\}^{1/2}} \sum_{n=1}^{N} C_n \sin(\psi_1 + \omega_g \Delta t_n)$$

$$E_3 = \frac{\Delta W_g}{U} \frac{(\omega_g/\omega)}{\omega^2\left\{\left[1 - (\omega_g/\omega)^2\right]^2 + 4(\omega_g/\omega)^2\zeta_T^2\right\}^{1/2}} \sum_{n=1}^{N} C_n e^{\omega\zeta_T \Delta t_n} \cos(\psi_2 + \omega \Delta t_n)$$

(4.50) start)

$$E_4 = \frac{\Delta W_g}{U} \frac{(\omega_g/\omega)}{\omega^2\left\{\left[1 - (\omega_g/\omega)^2\right]^2 + 4(\omega_g/\omega)^2\zeta_T^2\right\}^{1/2}} \sum_{n=1}^{N} C_n \, e^{\omega\zeta_T \Delta t_n} \sin(\psi_2 + \omega\Delta t_n)$$

$$\tan\psi_1 = \frac{2(\omega_g/\omega)\zeta_T}{1 - (\omega_g/\omega)^2} \quad ; \quad \tan\psi_2 = \frac{2\zeta_T}{1 - (\omega_g/\omega)^2} \qquad (4.50\ \text{concl.})$$

$$(\omega/\omega_g) = 1 + \epsilon \; ; \; |\epsilon| \ll 1 \; ; \; \zeta_T \neq 0$$

$$q_{\bar{\xi}}(t) = \sqrt{F_1^2 + F_2^2}\cos\left(\omega t - \arctan\frac{F_2}{F_1}\right) + e^{-\omega\zeta_T t}\sqrt{F_3^2 + F_4^2}\cos\left(\omega t - \arctan\frac{F_4}{F_3}\right)$$

$$F_1 = \frac{\Delta W_g}{U} \frac{1}{2\omega^2\zeta_T\left[1 + (\epsilon/\zeta_T)^2\right]^{1/2}} \sum_{n=1}^{N} C \cos\left(\omega\Delta t_n - \arctan\frac{\epsilon}{\zeta_T}\right)$$

$$F_2 = \frac{\Delta W_g}{U} \frac{1}{2\omega^2\zeta_T\left[1 + (\epsilon/\zeta_T)^2\right]^{1/2}} \sum_{n=1}^{N} C_n \sin\left(\omega\Delta t_n - \arctan\frac{\epsilon}{\zeta_T}\right)$$

$$F_3 = \frac{\Delta W_g}{U} \frac{1}{2\omega^2\zeta_T\left[1 + (\epsilon/\zeta_T)^2\right]^{1/2}} \sum_{n=1}^{N} C_n \, e^{\omega\zeta_T\Delta t_n} \cos\left(\omega\Delta t_n - \arctan\frac{\epsilon}{\zeta_T}\right)$$

$$F_4 = \frac{\Delta W_g}{U} \frac{1}{2\omega^2\zeta_T\left[1 + (\epsilon/\zeta_T)^2\right]^{1/2}} \sum_{n=1}^{N} C_n \, e^{\omega\zeta_T\Delta t_n} \sin\left(\omega\Delta t_n - \arctan\frac{\epsilon}{\zeta_T}\right)$$

(4.51)

Section 5
DISCUSSION OF RESULTS

5.1 GUST PENETRATION LOADS AND ELASTIC VEHICLE RESPONSE

The gust penetration load as a function of penetration depth into a sinusoidal gust is shown in Fig. 7. The command module load reaches steady state very fast and follows closely the gust wave shape, whereas the total gust load has a somewhat more involved dependence. Figure 7 defines the maximum gust penetration load ($|N|_{max}$) as related to the critical gust penetration depth ($\bar{U}t^*$) into a sinusoidal gust. The transient load response at gust penetration does apparently not constitute the worst load condition which is in agreement with the findings of other investigators (Refs. 13 and 17).

The actual positions of the launch vehicle in the sinusoidal gust for peak and bottom values of $|N|_{max}$ are sketched in the insets of Fig. 8. The effect of neglecting to account for the fact that the convection velocity is less than free stream velocity in regions of separated flow ($\kappa \neq 1$) is negligible for the Saturn V gust penetration load. That is, using experimental static data in the classical quasi-steady theory will give good prediction of the gust penetration load. One would still not expect attached flow theories to give a realistic prediction. It is, therefore, rather surprising to find that the Saturn-V gust penetration load at maximum dynamic pressure is very well predicted by the attached flow theory used by Glau and Blackburn (Fig. 9). It is obvious that the good agreement is fortuitous. The theoretical load distribution, although deviating very substantially from the measured distribution, happens to give the same total C_{N_α} (Figure 3). As the wave length decreases the difference in load distribution starts to show up ($L_b/L_g > 1.25$ in Figure 9). Likewise the gust induced bending moment on the elastic vehicle would be sensitive to the load distribution, and the agreement shown in Figure 9 would never be realized.

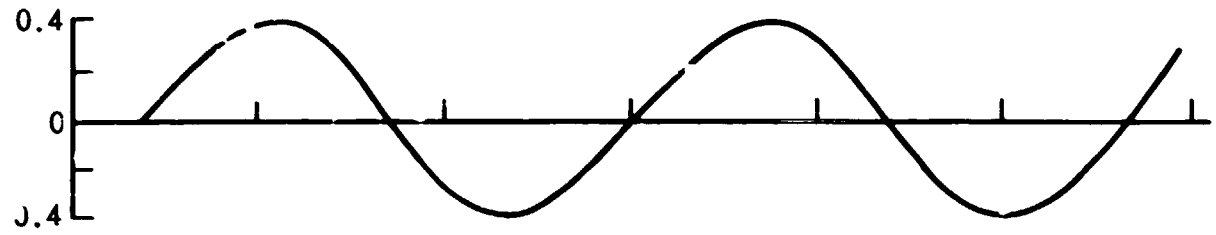

c. COMMAND MODULE

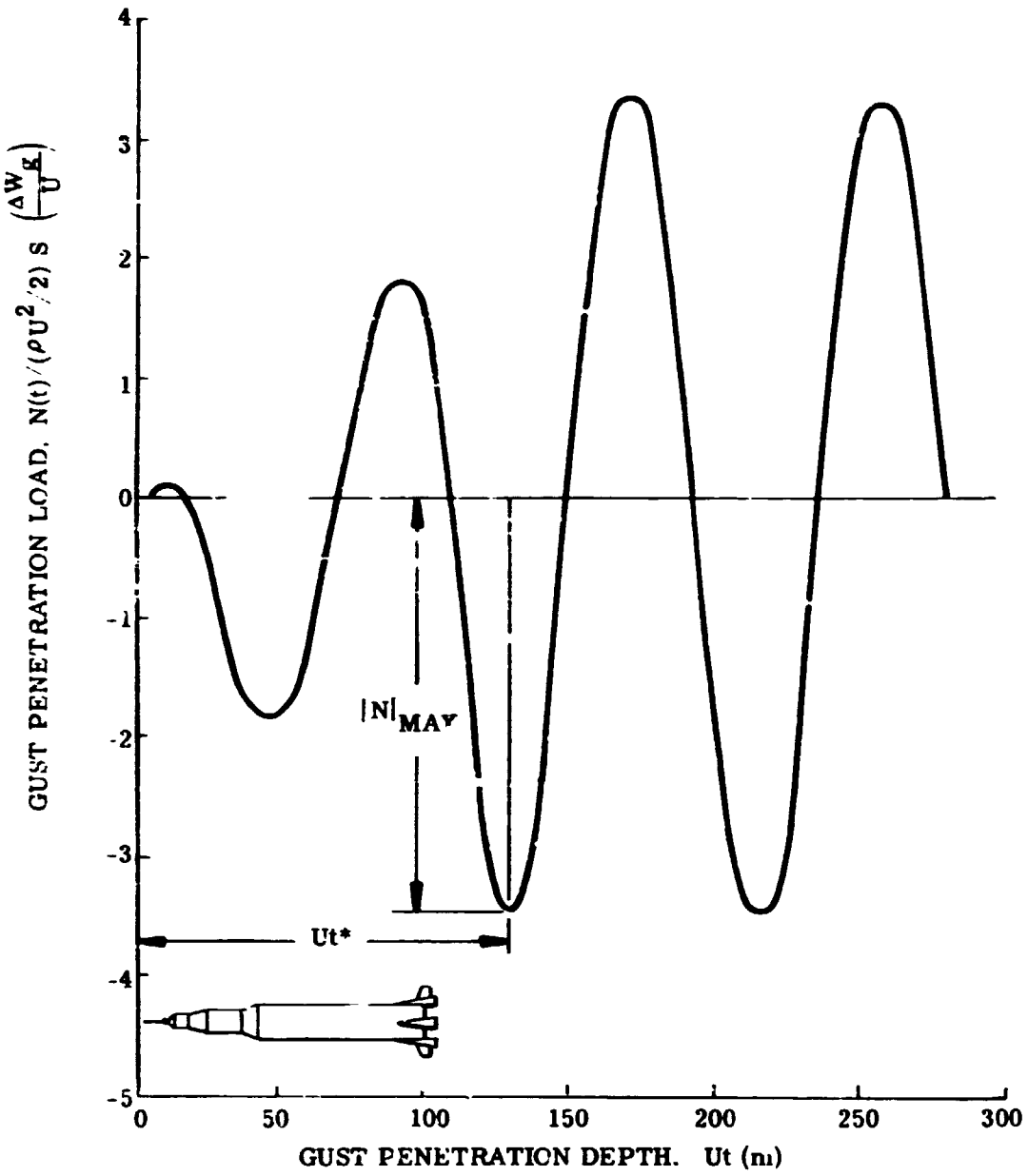

b. TOTAL VEHICLE

Fig. 7 Saturn-V Gust Penetration Load as a Function of Penetration Depth Into a Sinusoidal Gust (L_b/L_g = 1.0), at Maximum Dynamic Pressure (M = 1.6)

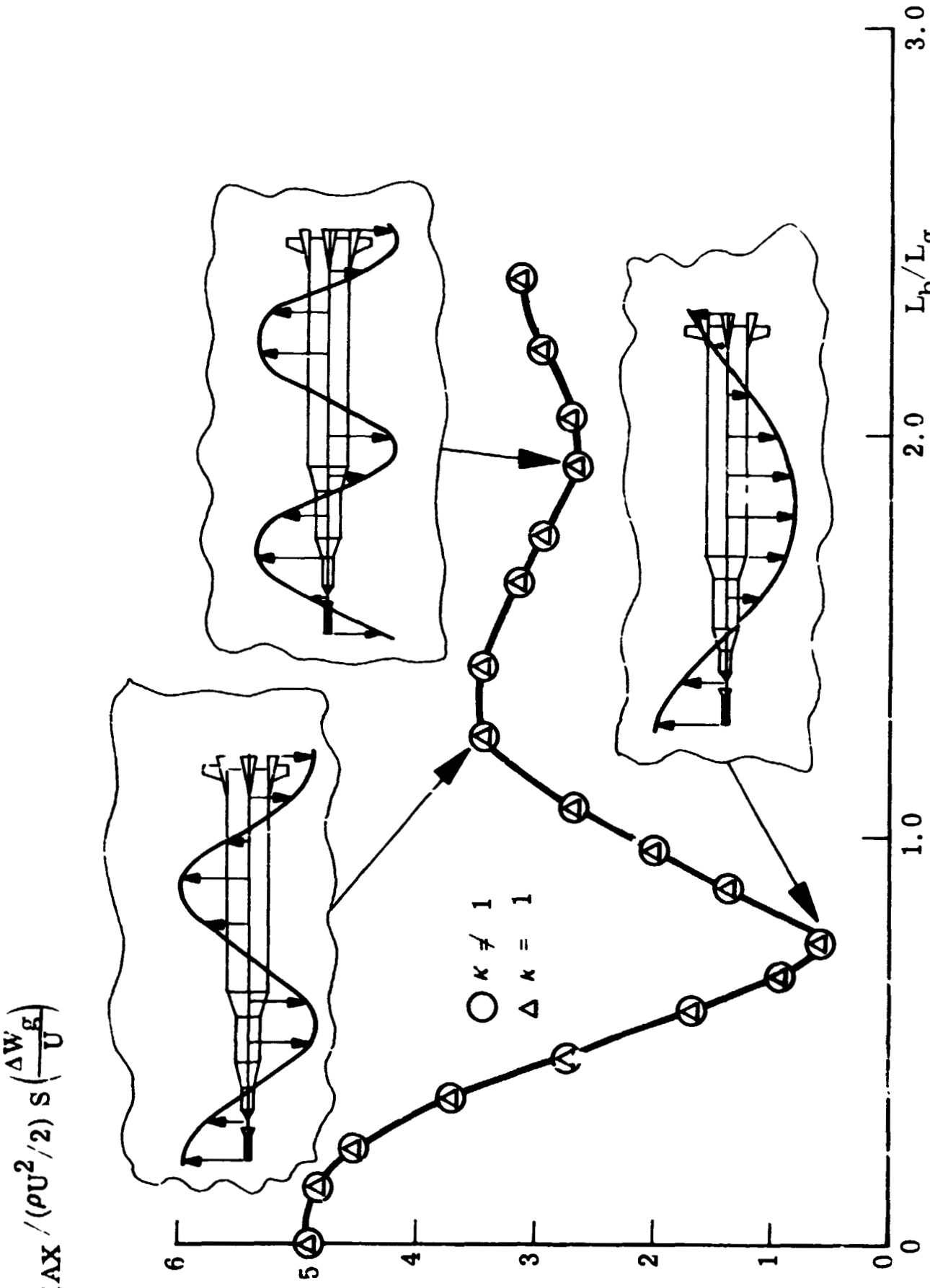

Fig. 8 Saturn-V Maximum Gust Penetration Load as a Function of Gust Wave Length at M = 1.6

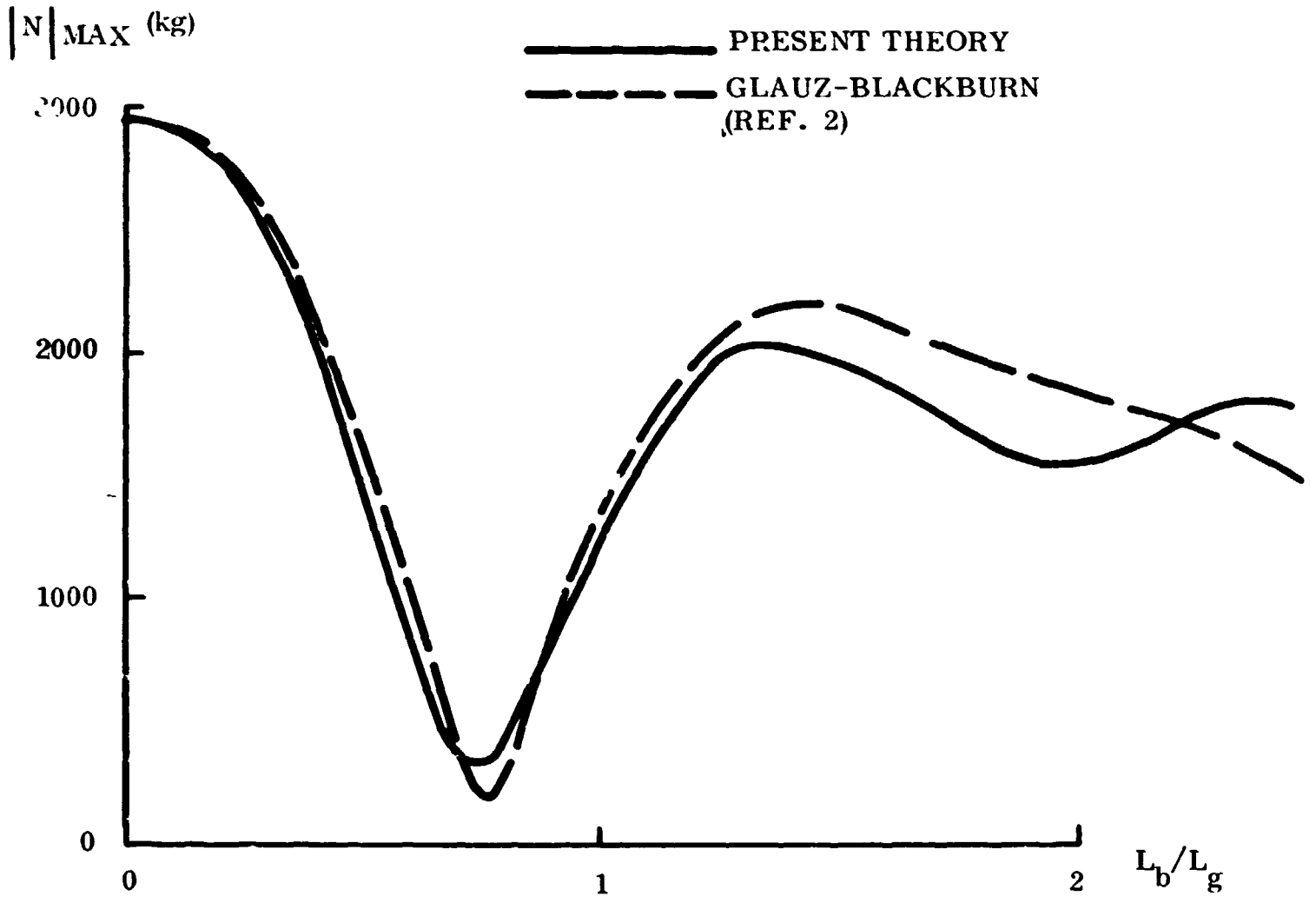

Fig. 9 Saturn-V Gust Penetration Load at Maximum Dynamic Pressure (M = 1.6)

The gust penetration load $|N|_{max}$ is of concern only when the rigid body response is considered.

The elastic vehicle response of the Saturn V (AS-508) is shown in Fig. 10. Again, it is only after full penetration into the sinusoidal gust that maximum gust-induced bending moment (Fig. 10a) and amplitude response (Fig. 10b) are obtained. Notice, however, that the steady state amplitude response is approached from above, as could be expected from examination of Eqs. (4.56) and (4.57). Thus, it is the transient elastic vehicle response that gives the maximum amplitude response, and only two consecutive sinusoidal gust waves are needed to reach maximum amplitude. The beat of the amplitude response (compare $\Delta\phi_N$, Fig. 10b, with P(t), Fig. 10a) is caused by the off-resonance gust frequency ($\omega_g/\omega = 0.6$). The variation of these maximum gust responses with sinusoidal gust wavelength is shown in Fig. 11. The launch vehicle positions in the gust wave for the "peaks and valleys" of the maximum gust-induced bending moment are shown in the insets of Fig. 11a.

Comparing Figs. 11a and 11b, one notices with some concern that the gust-induced moment at resonance is near maximum, resulting in close to the maximum possible response. It is apparent from Fig. 11b that the off-resonance response is an order of magnitude smaller than the response at resonance. As before, for the (Saturn V) gust penetration load, $\kappa = 1$ versus $\kappa \neq 1$ is found to have no measurable effect on the amplitude response. The same is true about the effect of structural damping on the off-resonance response. At resonance, the effect of damping is of course, dominant (Eq. (4.57).

On the Saturn I vehicle the effect of neglecting the difference in free stream and separated flow convection velocities, $\kappa \neq 1$ compared to $\kappa = 1$, is no longer small (Fig. 12). Comparing Fig. 12a and 12b, one can see that the gust-induced bending moment is not near its peak for the resonant gust wavelength. As a consequence, the elastic vehicle response at resonance is not the maximum possible.

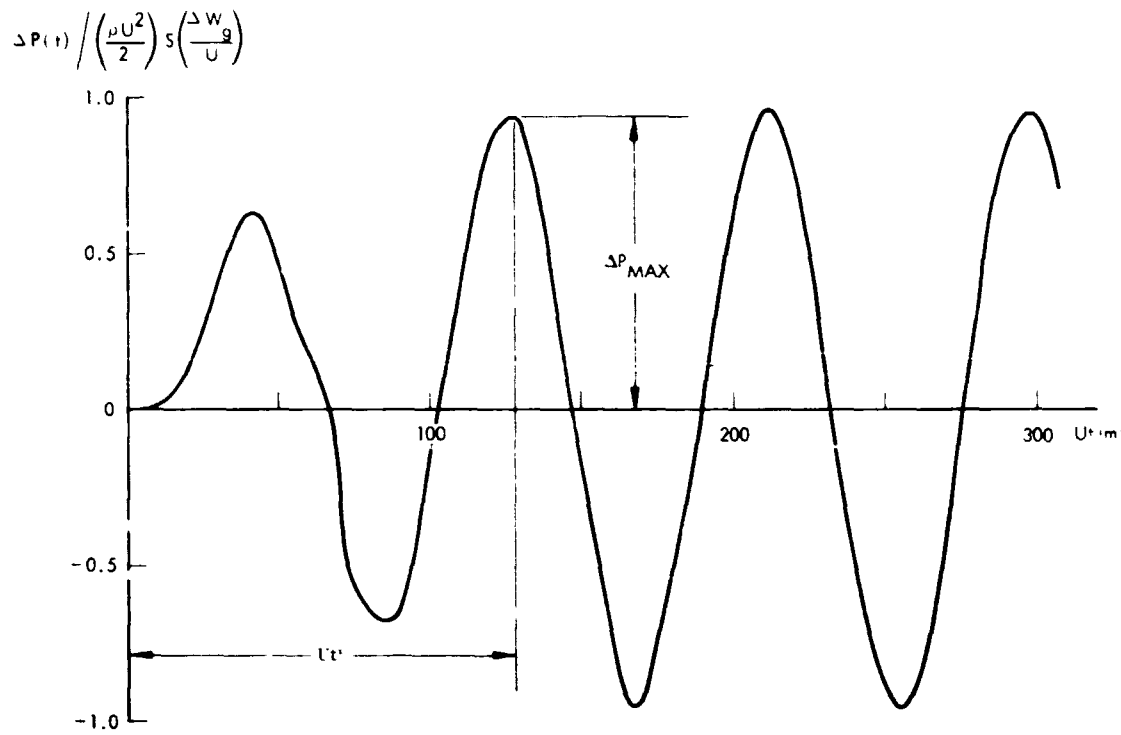

a. Gust-Induced Bending Moment (1st B.M.)

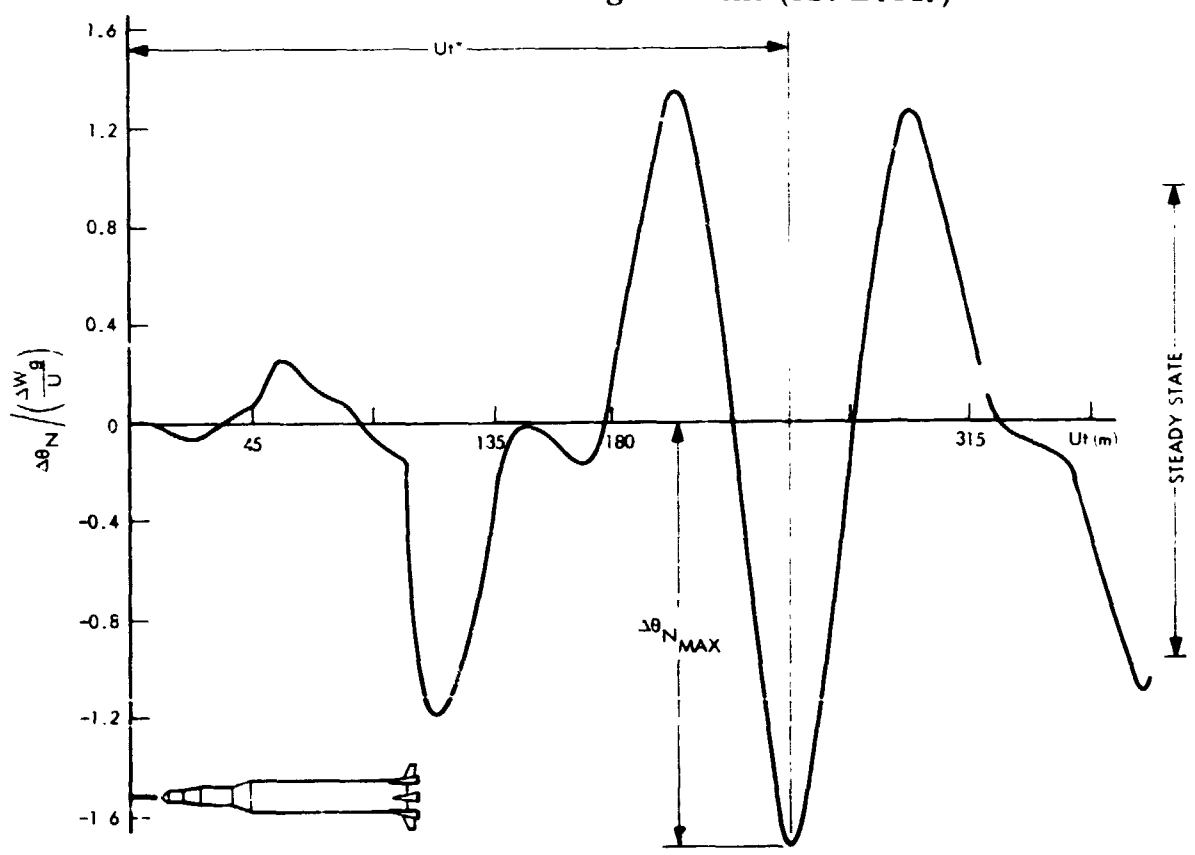

b. Elastic Vehicle Response (1st B.M.)

Fig. 10 Saturn-V (AS-508) Elastic Body Gust Penetration Effects as a Function of Penetration Depth into Sinusoidal Gusts (L_b/L_g = 1.05) at Maximum Dynamic Pressure (M = 1.6)

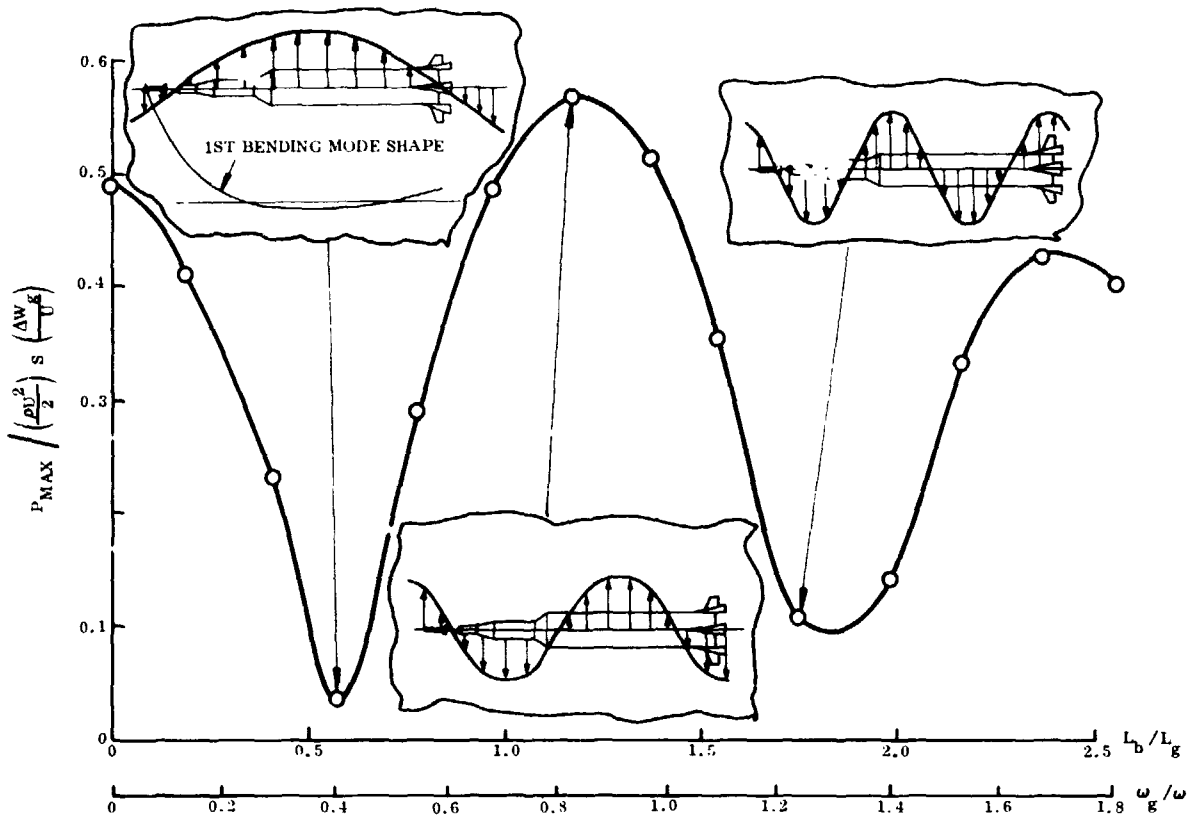

a. Maximum Gust-Induced Bending Moment (1st B. M.)

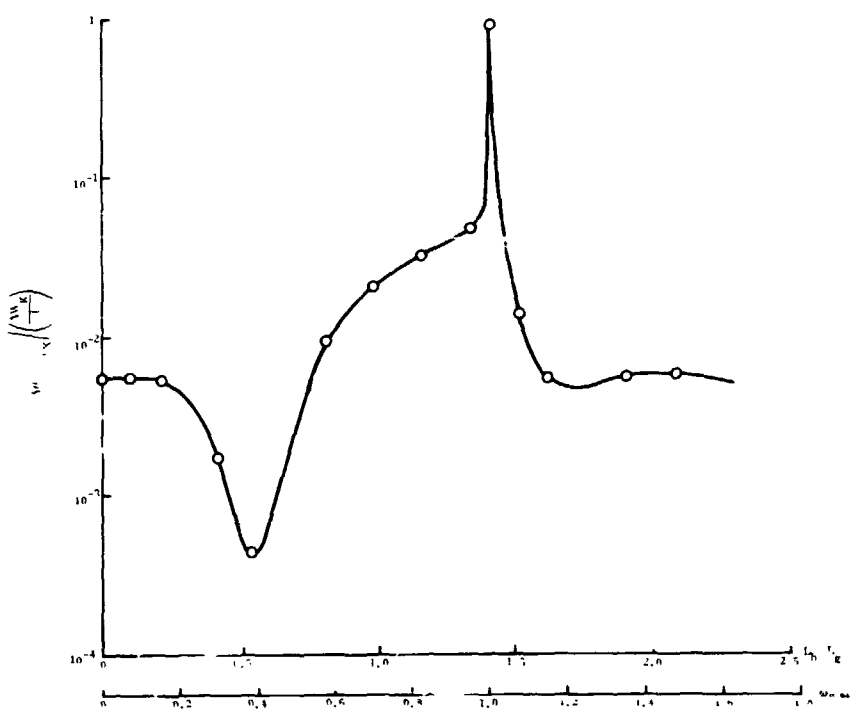

b. Maximum Elastic Vehicle Response (1st B. M., $\zeta = 0$)

(AS-508) Maximum Elastic Body Gust Penetration Effects as a Function of Sinusoidal Gust Wave Length (M = 1.6)

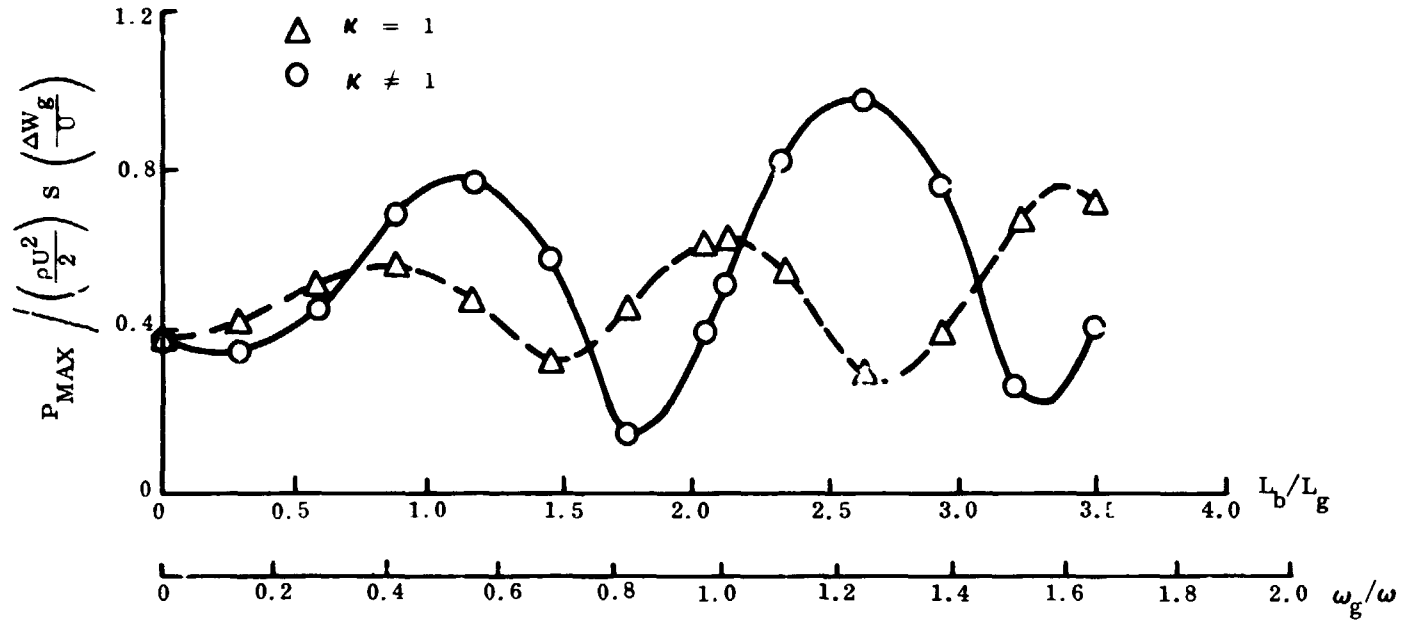

a. MAXIMUM GUST-INDUCED BENDING MOMENT (1ST B.M.)

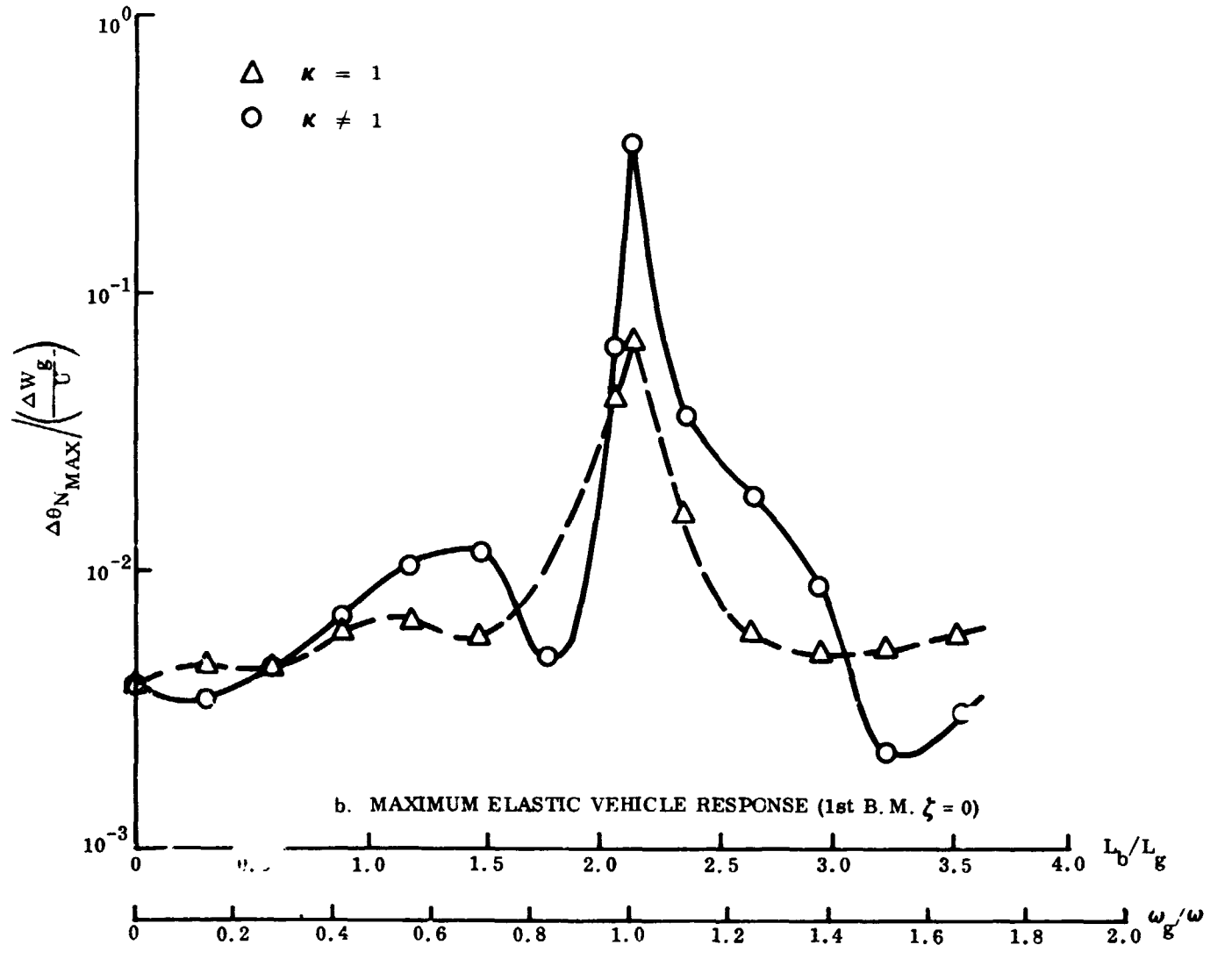

b. MAXIMUM ELASTIC VEHICLE RESPONSE (1st B.M. $\zeta = 0$)

Figure 12 Maximum Elastic Body Gust Penetration Effects of the Saturn I Launch Vehicle with Disk-On Escape Rocket at M = 0.9

That is, the maximum possible response at resonance is substantially higher than that shown in Fig. 12. It would be reached if the structural rigidity was changed such that the gust-induced moment reached a maximum when the gust wavelength gave resonance conditions for one of the bending mode. For a simple geometry, as the one sketched in Fig. 13, the critical stiffness and associated natural body bending frequency giving maximum elastic vehicle gust response at resonance can be determined very simply.

At resonance

$$\omega = \omega_g = 2\pi U/L_g \tag{5.1}$$

That is,

$$\omega L_g/2\pi U = 1 \tag{5.2}$$

The maximum gust-induced bending moment occurs when the gust-induced crossflow is distributed as shown in Fig. 13. That is, the maximum elastic vehicle response at resonance will occur when the characteristic body length L_b^* (where $L_b^* \approx L_b$) is related to the gust wavelength L_g as follows (σ = 1, 2, 3, etc.):

$$L_b^*/L_g = \begin{cases} \sigma & : \text{ Odd No. B.M.} \\ \sigma + 1/2 & : \text{ Even No. B.M.} \end{cases} \tag{5.3}$$

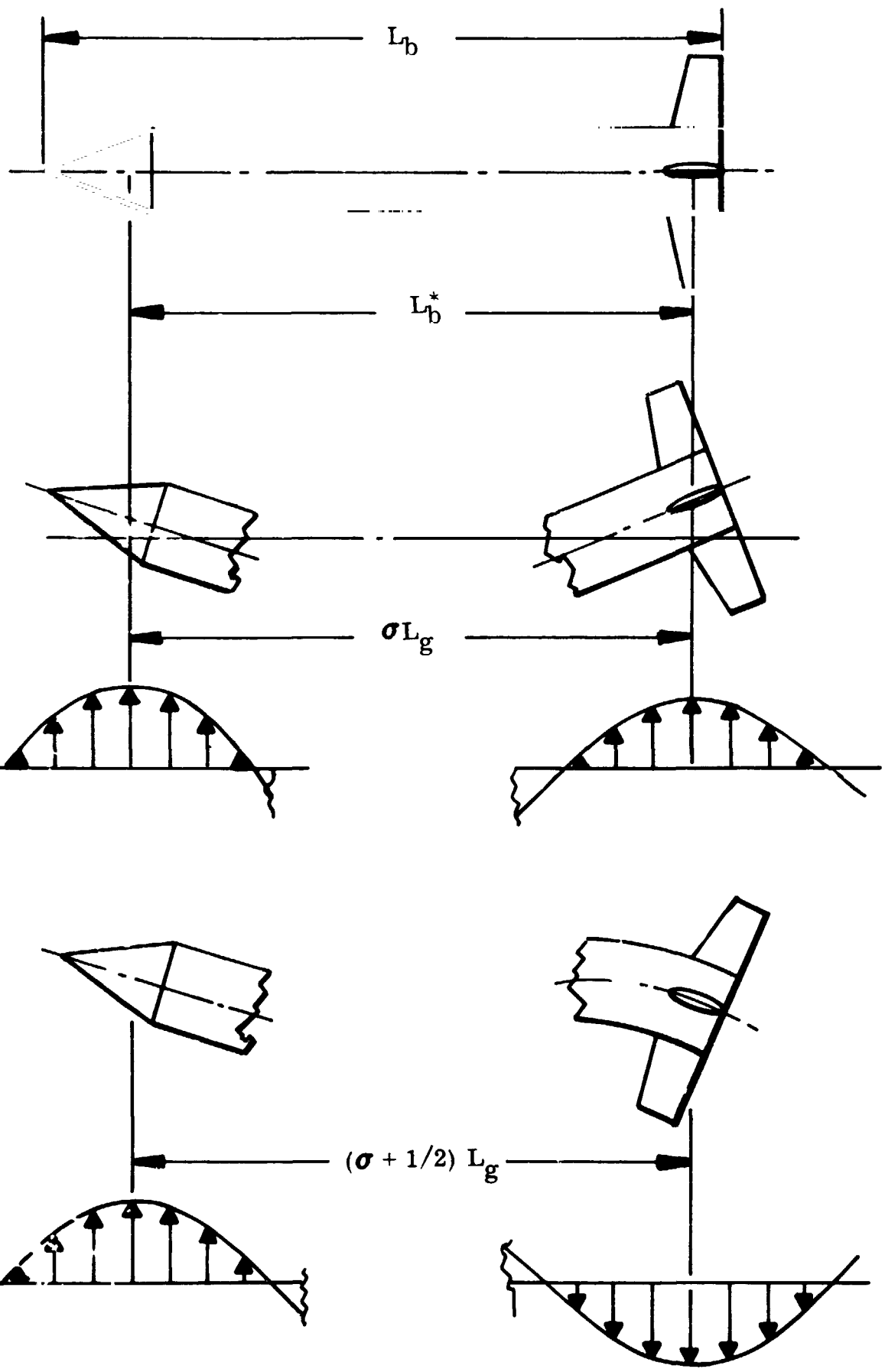

Fig. 13 Critical Gust Wave Lengths of Resonance

Conversely, the minimum gust-induced response at resonance will be obtained when

$$L_b^*/L_g = \begin{cases} \sigma + 1/2 & : \quad \text{Odd No. B.M.} \\ \sigma & : \quad \text{Even No. B.M.} \end{cases} \tag{5.4}$$

Thus, a critical Strouhal number S* giving maximum elastic vehicle response to sinusoidal gusts (at resonance) can be defined as foilows:

$$S^*_{crit} = \frac{(\omega/2\,\pi)\,L_b^*}{U} = \begin{cases} \sigma & : \quad \text{Odd No. B.M.} \\ \sigma + 1/2 & : \quad \text{Even No. B.M.} \end{cases} \tag{5.5}$$

It would obviously be wise to design the launch vehicle such that the structural rigidity did not generate a critical Strouhal number, especially not for any of the lower bending modes. The increasing dominance of structural damping with increasing natural bending frequency makes the higher mode shapes less prone to exhibit any large amplitude response.

The goal should, of course, be to get as close as possible to the optimum stiffness – that giving minimum gust response at resonance – which is given by the optimum Strouhal number defined below

$$S^*_{opt} = \frac{(\omega/2\,\pi)\,L_b^*}{U} = \begin{cases} \sigma + 1/2 & : \quad \text{Odd No. B.M.} \\ \sigma & : \quad \text{Even No. B.M.} \end{cases} \tag{5.6}$$

The simple geometry sketched in Fig. 13 represents a great number of military missiles and civilian launch vehicles. Of the Apollo-Saturn launch vehicles, however, it is only vehicles AS-203, AS-206, and AS-208 that fall in that category. The other Saturn boosters have more complicated geometries, and the maximum (and minimum) possible elastic vehicle response at resonance can be determined only through more involved

computations. First, the wavelengths giving maximum (and minimum) gust-induced bending moments are determined, and the resonant vehicle response is then computed using the (fictitious) bending mode frequency corresponding to resonance conditions at these critical gust wavelengths.

Figure 14 shows how these maximum and minimum possible responses at resonance compare with those predicted using the actual bending mode characteristics. Figure 14a shows the data for the Saturn V (AS-508) vehicle, and in Fig. 14b the data for Saturn I with dick-on escape rocket is shown. It appears that for the Saturn I vehicle the structural stiffness is not far from the optimum one giving minimum elastic vehicle response at resonance (Fig. 14b). However, for the Saturn V vehicle, the structural stiffness is found to be close to the value giving maximum gust response. It is interesting to note that even the minimum possible elastic vehicle gust response at resonance generally is higher than all off-resonance gust response (Compare Figs. 14a and 12b). That is, the elastic vehicle response at resonance will always produce the critical gust design loads.

Off resonance the maximum elastic vehicle gust response varies with the gust wavelength only via the forcing function, i.e., the gust induced bending moment (See Figs. 11 and 12). Thus, where the gust wavelength becomes much larger than the body length and the bending moment varies monotonically with increasing gust wavelength, one would not expect to see any response "wiggles." It is therefore difficult to see any aerodynamic (or structural) source for the oscillatory behavior of Papadopoulos' results at low gust frequencies (Ref. 26 and Fig. 15). Consequently, not much significance should be attributed to the fact that the present predictions coincide with the minimum off-resonance response predicted by Papadopoulos. There is, of course, no reason to expect the two predictions to agree, since Papadopoulos used attached flow "quasi-steady"* aerodynamics in which the effects separated flow load modification and separated flow time lag were neglected. It should be noted that the measured gimbal engine response does not show any low-frequency wiggies (Ref. 26 and Fig. 16).** Comparing Figs. 15 and 16, one would have to conclude that the present method would have given better agreement with the experimental results.

---

*In the classical sense

** The flight data scatter around a fairly constant level

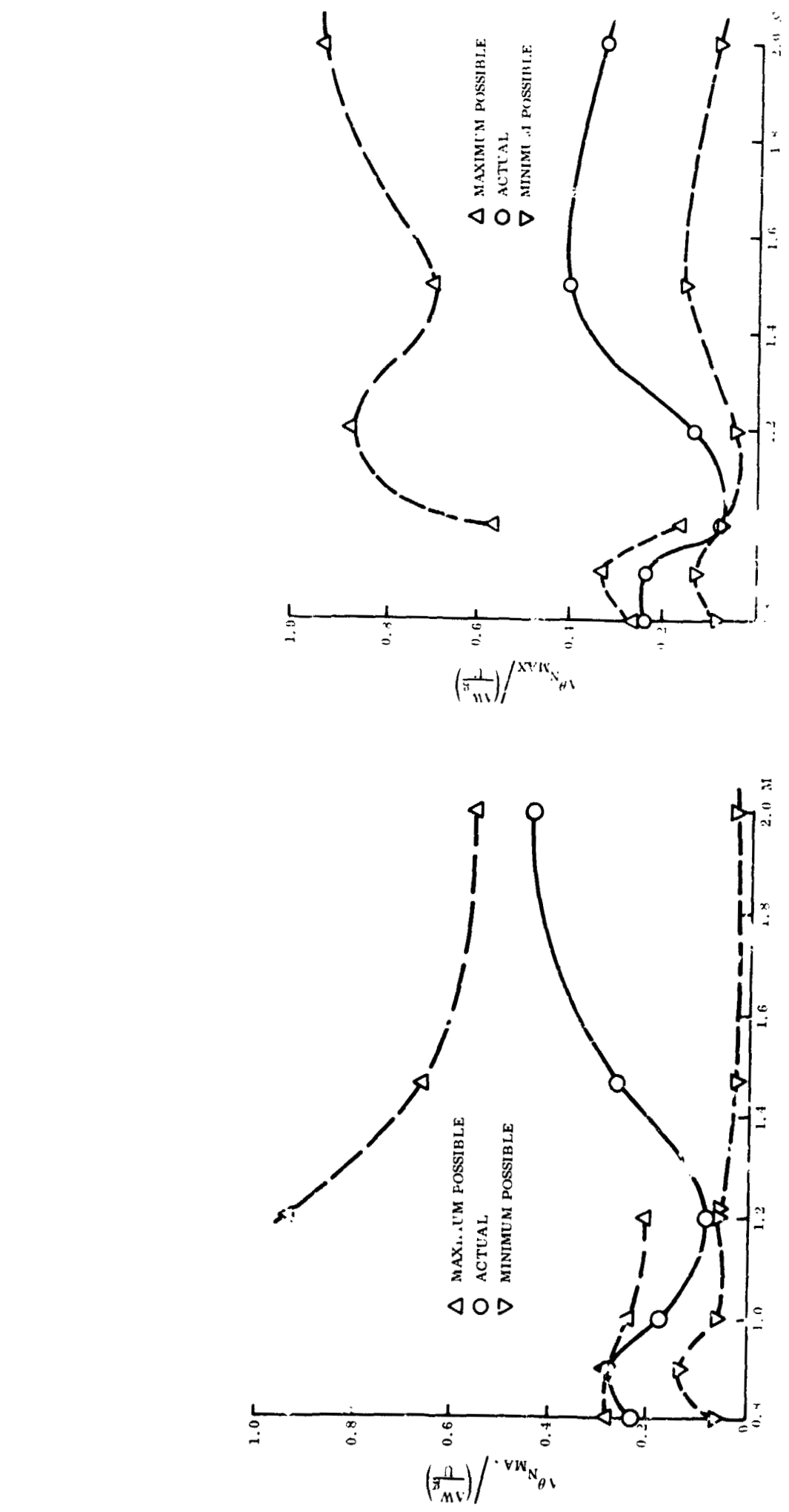

a Saturn-V (AS 508) Launch Vehicle

b. Saturn-I Launch Vehicle With Disk-On Escape Rocket

Fig. 14 Maximum, Minimum, and Actual Sinusoidal Gust Response at Resonance as a Function of Mach Number (1st B.M., $\zeta = 0.01$)

N-3C-70-2

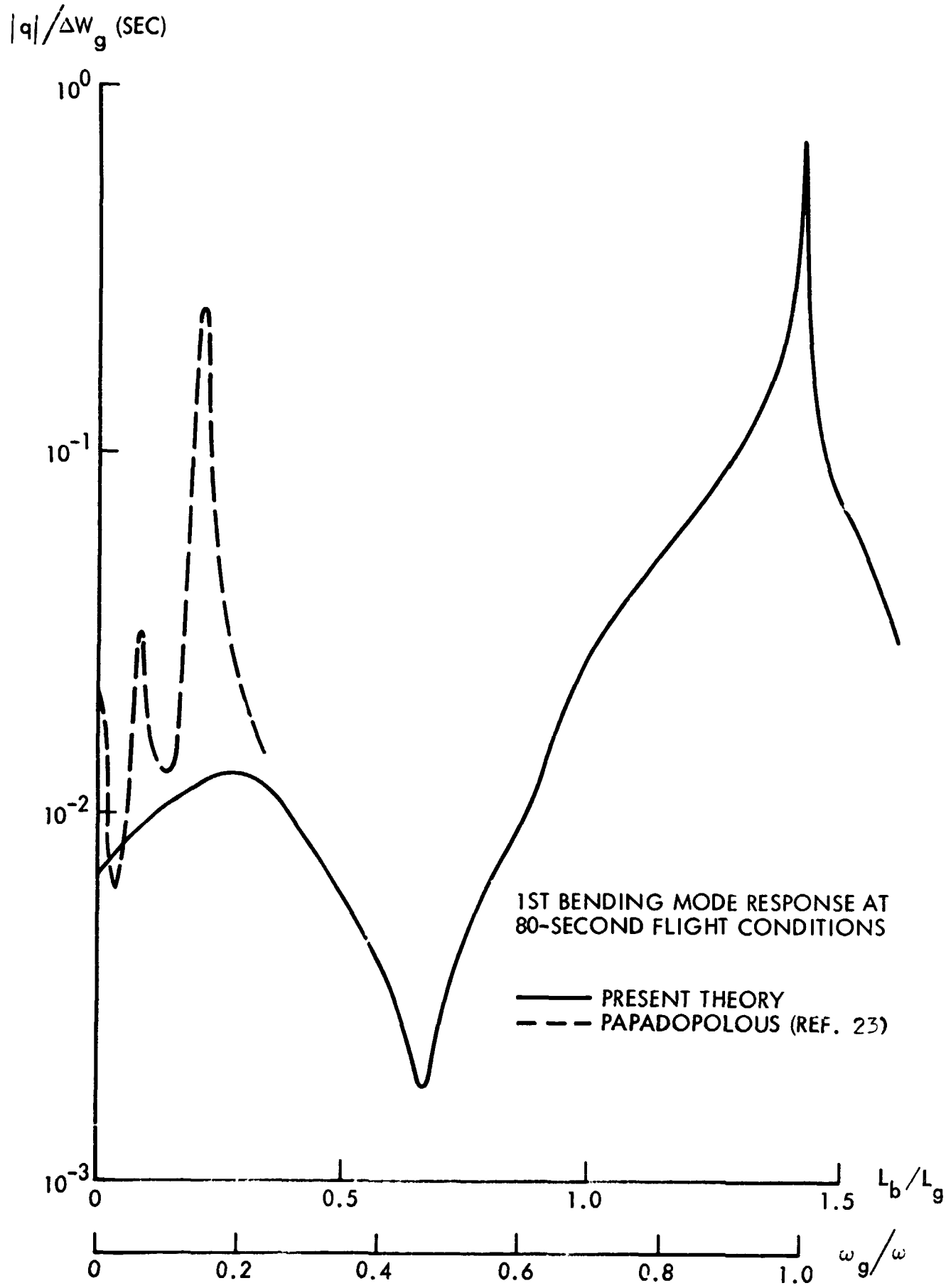

Fig. 15 Saturn-I (AS-9) Elastic Vehicle Response to Sinusoidal Gusts as Determined by Present and Previous Theories (1st B.M.)

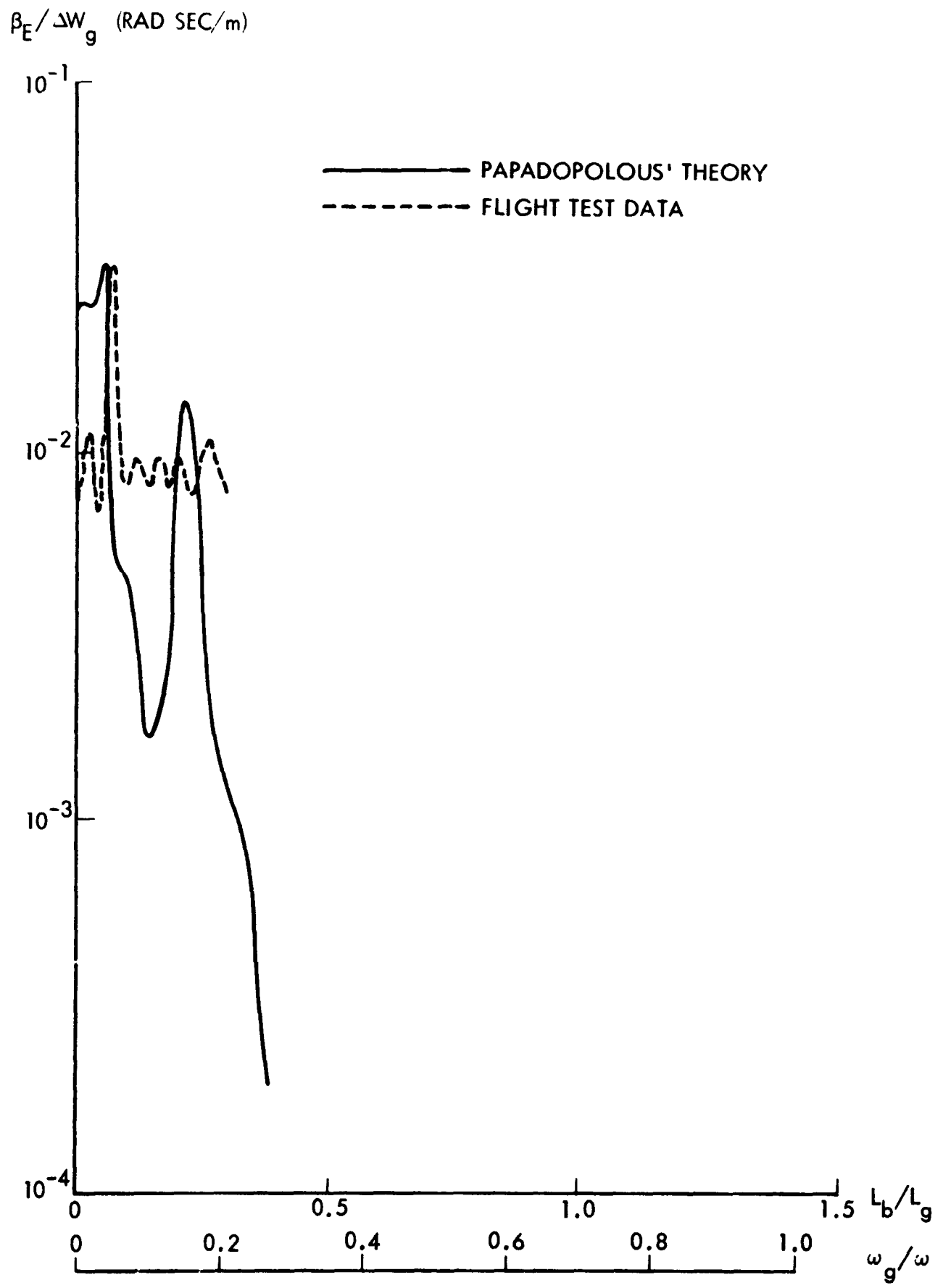

Fig. 16 Saturn-I (AS-9) Gimbal Engine Response to Sinusoidal Gusts (Ref. 26)

The measured sinusoidal gusts in the earth's atmosphere can be represented in statistical form, as shown in Fig. 17 (Refs. 22 and 27). According to these data, the AS-508 vehicle would experience the gust induced nose amplitudes shown in Fig. 18. The figure shows the maximum response off resonance, i.e., the maximum dynamic pressure data of Fig. 11b converted into real loads and deflections by use of the data in Fig. 17.

Figure 19 shows the response at resonance after penetration through the maximum number of gust cycles (ν_{max}) given by Fig. 17. The effect of structural damping on the response at resonance is large, as could be expected. Equation (4.51) shows that the response amplitude is inversely proportional to the total damping, structural plus aerodynamic. The effect of finite ν_{max} is not noticeable, as the maximum response is obtained within a couple of cycles (see Fig. 10b).

The nose-deflection amplitudes $\Delta\theta_N^\circ$, shown in Figs. 18 and 19, are large, especially at resonance. To determine whether or not they are large enough to endanger the structural integrity of the launch vehicle is outside of the scope of the present investigation. However, it certainly appears that the effects of sinusoidal gusts on Saturn V class launch vehicles are serious enough to be cause for concern.

Without the effects of sinusoidal gusts, the structural integrity of the Saturn V launch vehicles AS-505 through AS-508 would never be endangered. The vehicles are aeroelastically stable throughout atmospheric ascent, as is shown in Appendix B.

The high-frequency gust response can be described using statistical methods (Refs. 16, 28, and 29). Before further improvements are sought in description of atmospheric turbulence, random gusts, and the like, the local unsteady flow on the launch vehicle surface should be better understood, especially when there are numerous regions with shock-boundary layer interaction.

5.2 COUPLING BETWEEN REGIONS OF SEPARATED FLOW

It is usually assumed that the fluctuating pressures and associated high frequency panel loads in one separated flow region are independent of the loads in adjacent separated

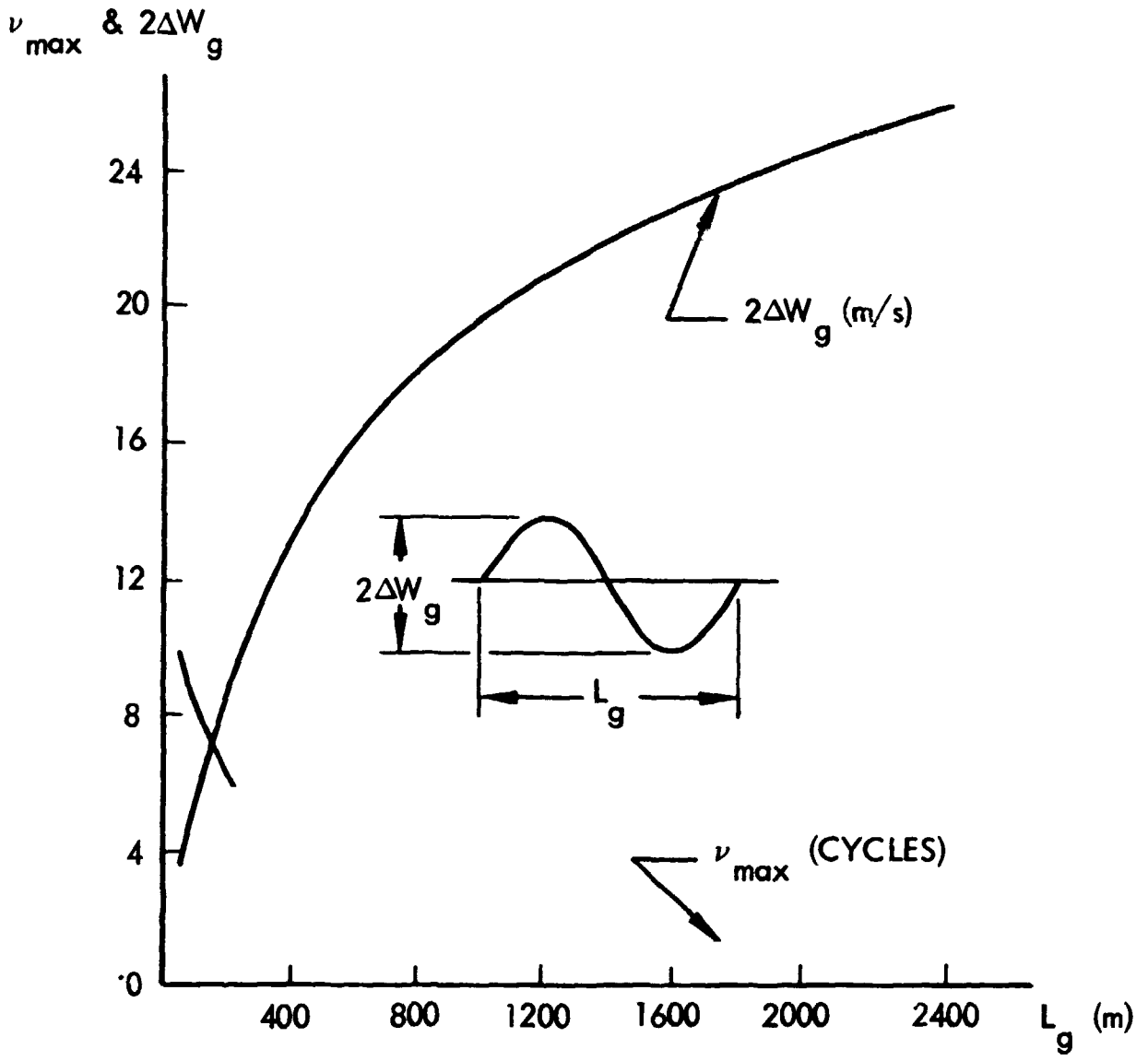

Fig. 17 Atmospheric Gust Amplitude and Frequency Data for Sinusoidal Gusts (Ref. 27)

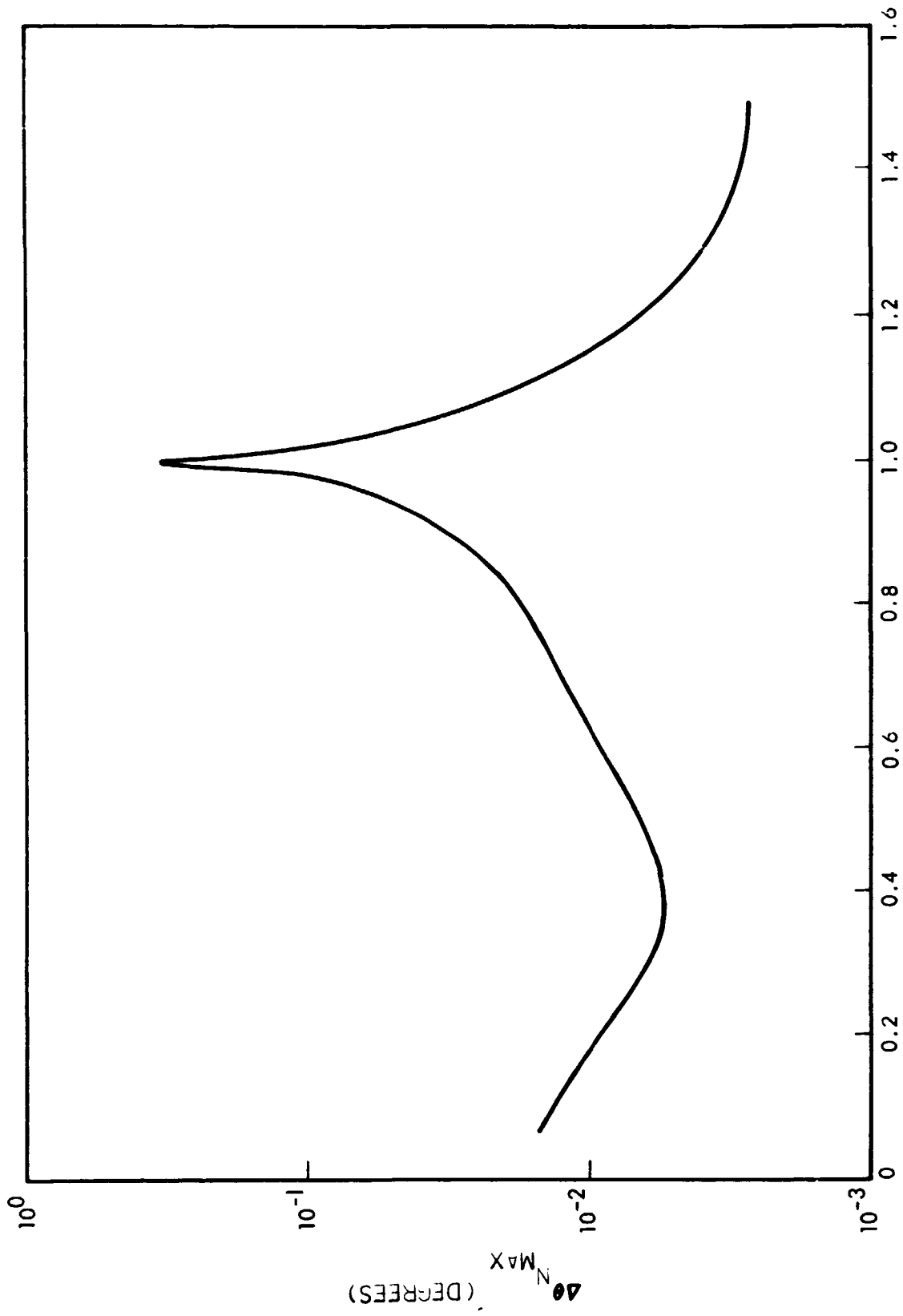

Fig. 18 Saturn-V (AS-508) Maximum Elastic Vehicle Response as a Function of Sinusoidal Gust Wave Length at Maximum Dynamic Pressure (1st B.M., ζ = 0.01, M = 1.6)

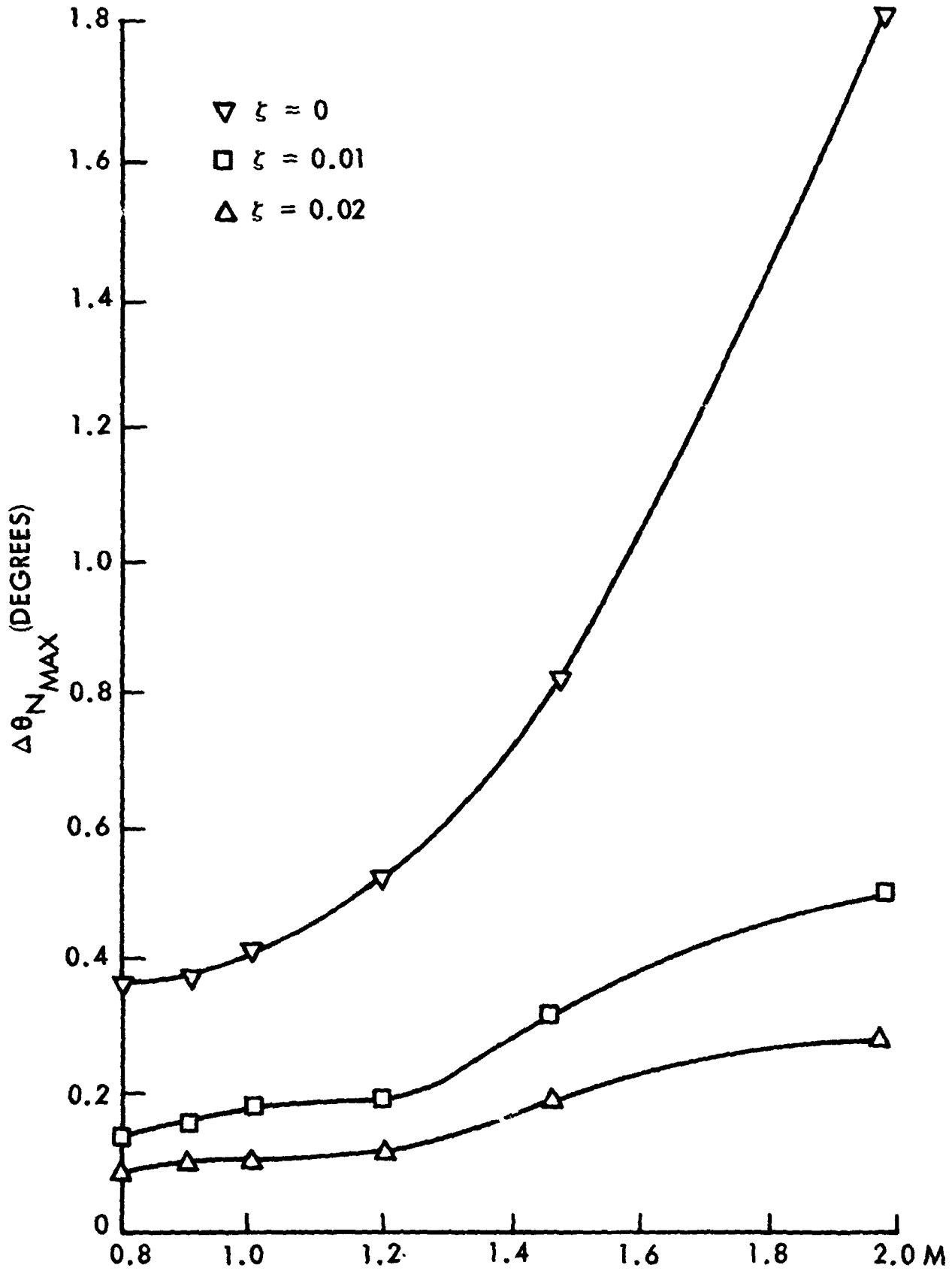

Fig. 19 Saturn-V (AS-508) Elastic Vehicle Gust Response at Resonance after Penetration of ν_{max} Sinusoidal Gust Cycles (1st B. M.)

flow regions. There now exists, however, strong evidence that this is not a very good assumption since in many cases there will be a strong coupling between separated flow regions.

Vorticity is generated in regions of shock-induced boundary layer separation (Refs. 5, 30-34), as is illustrated by Fig. 20. Usually the vorticity is contained in the viscous flow region and remains entrained in the boundary layer after reattachment. The flow photograph in Fig. 20a certainly indicates this to be the case. Ginoux (Ref. 33) has shown that the boundary layer retains a "long memory" of such vorticity, and that in regions of concavely curving flow the residual vorticity is amplified greatly. Thus, flow separations with their inherent concave flow curvature will re-establish and amplify pre-existing vorticity.

The implication of this is that for successive regions of shock-induced separation, as on AS-206 in Fig. 21 the vorticity generated by the first separated flow bubble will set the pattern for the vorticity generated at each successive separated flow region (Ref. 7). Analysis of static and dynamic experimental data (Ref. 7) gave substantiating evidence for this flow hypothesis. The bulk of the experimental results were obtained on a 25° – 10° biconic nose with a corrugated cylindrical aft body (Fig. 21a). The nose configuration was quite similar to that of the AS-206 vehicle (25° – 9° biconic nose, Ref. 35) and the separated flow field was, as a consequence, also quite similar (Fig. 21b).* The "preseparation" at the first shoulder generated a reattaching strong boundary layer forward of the second shoulder preventing the sudden complete leeward side separation with its attendent adverse aeroelastic effects (Refs. 35 and 36).

The fluctuating pressure measurements aft of the second shoulder (Fig. 22) show the shock-oscillation-imparted increased low-frequency content in the spectrum for the separated flow under the lambda foot of the normal shock, whereas the flow before and aft of the shock shows the usual boundary layer type spectra with relatively less low frequency content. Examination of the spectra around the circumference reveals that the position of the shock wave varies circumferentially (the forward leg for the lambda somewhat more than the terminal shock, Fig. 23). This is most likely the result of the

*Unfortunately, the Schlieren movies of the test were unsuitable for reproduction.

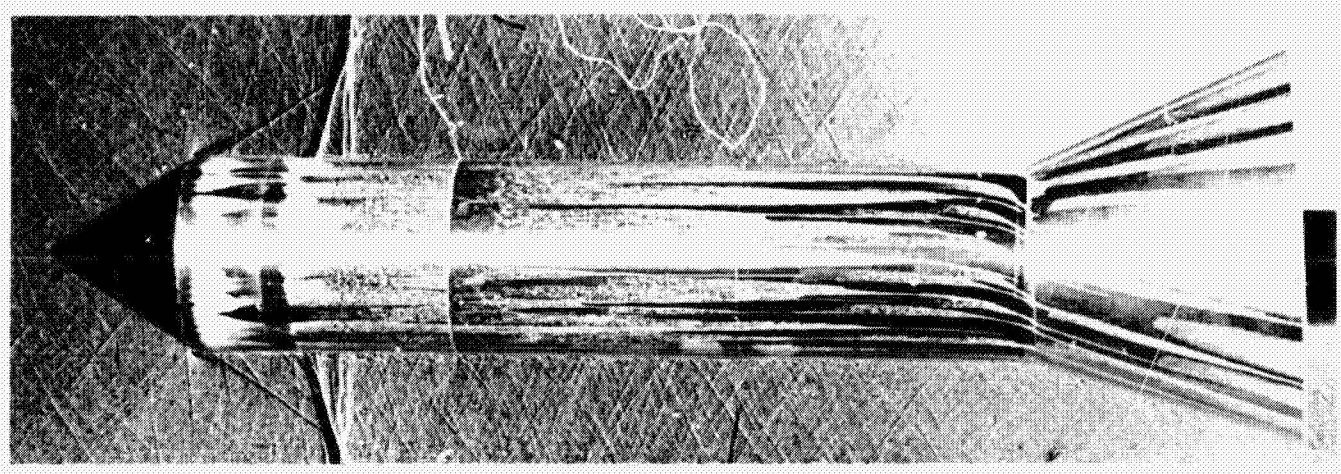

a. Long Cylinder-Body (M = 0.9)

b. Short Cylinder-Body (M = 1.2)

Fig. 20 Shock-Induced Boundary-Layer Separation on Cone-Cylinder-Flare Bodies

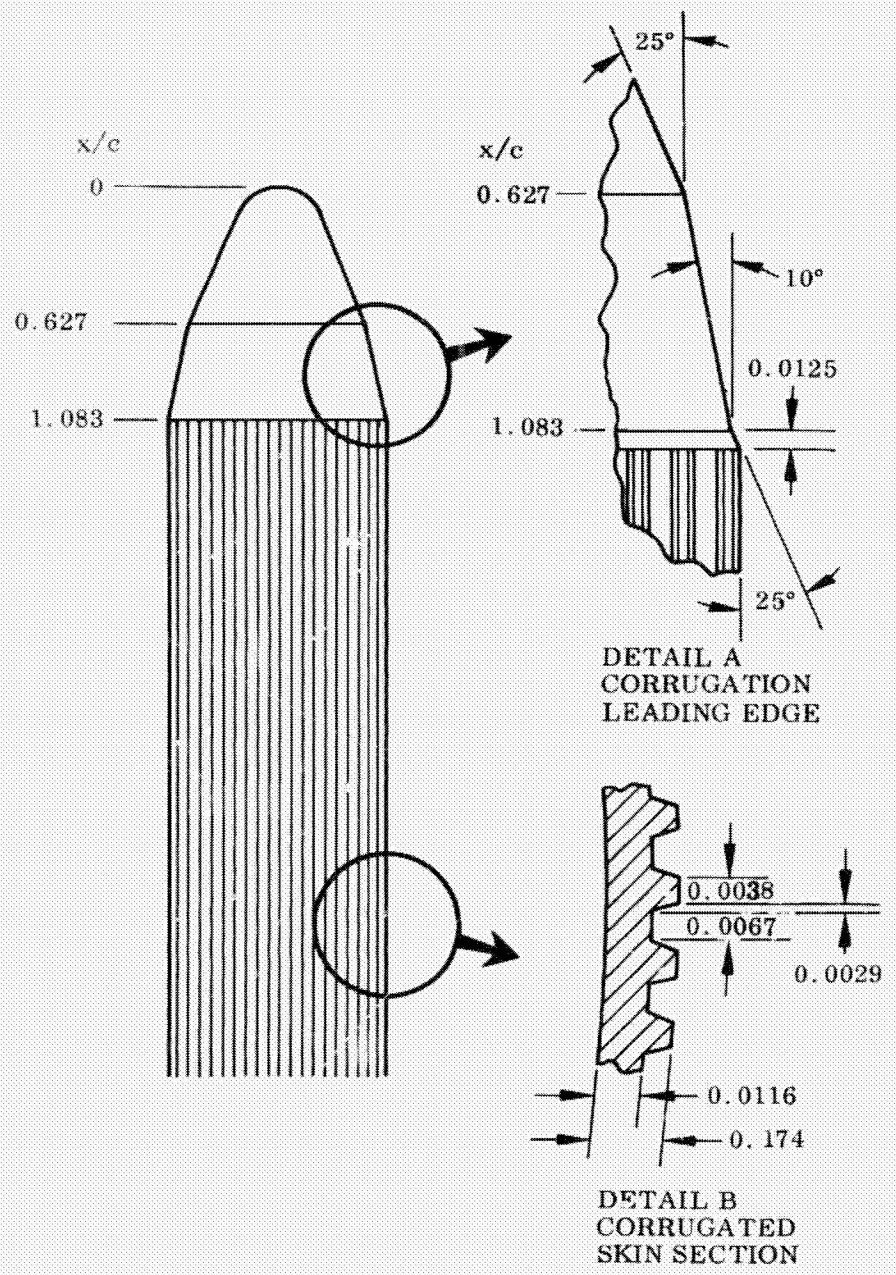

a. Model Used

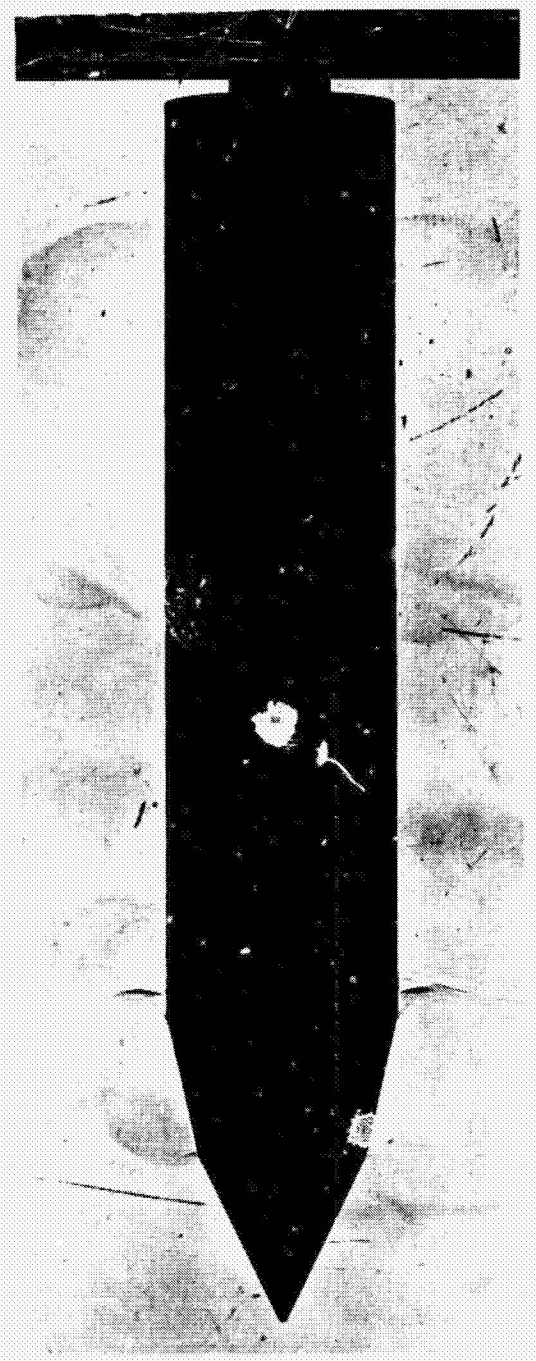

b. SA-206 Nose Geometry

Fig. 21 Multiple Regions of Shock-Induced Boundary-Layer Separation on Biconic-Nose-Cylinder Bodies

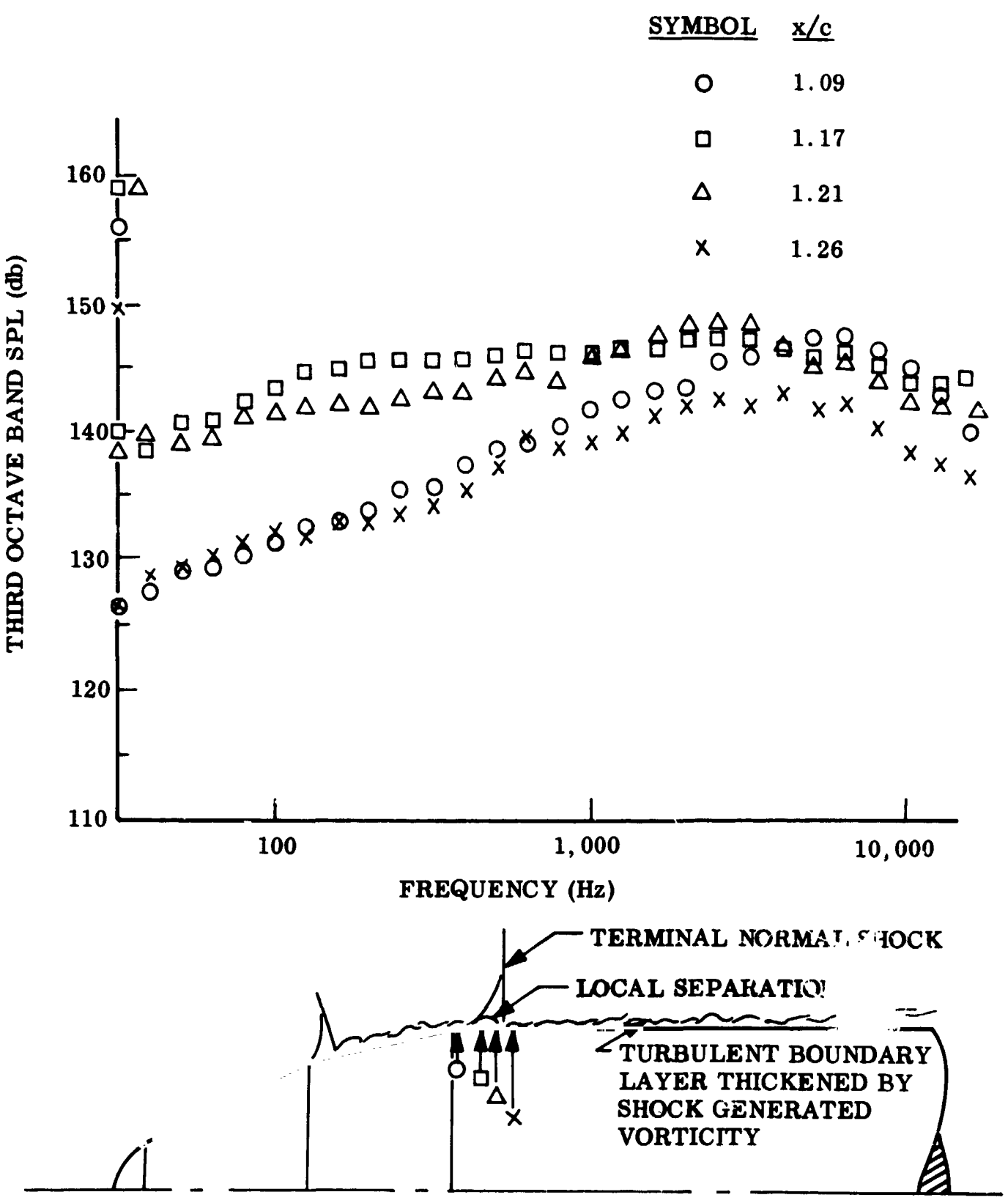

Fig. 22 Spectra in the Vicinity of a Terminal Normal Shock at M = 0.8 and α = 2°

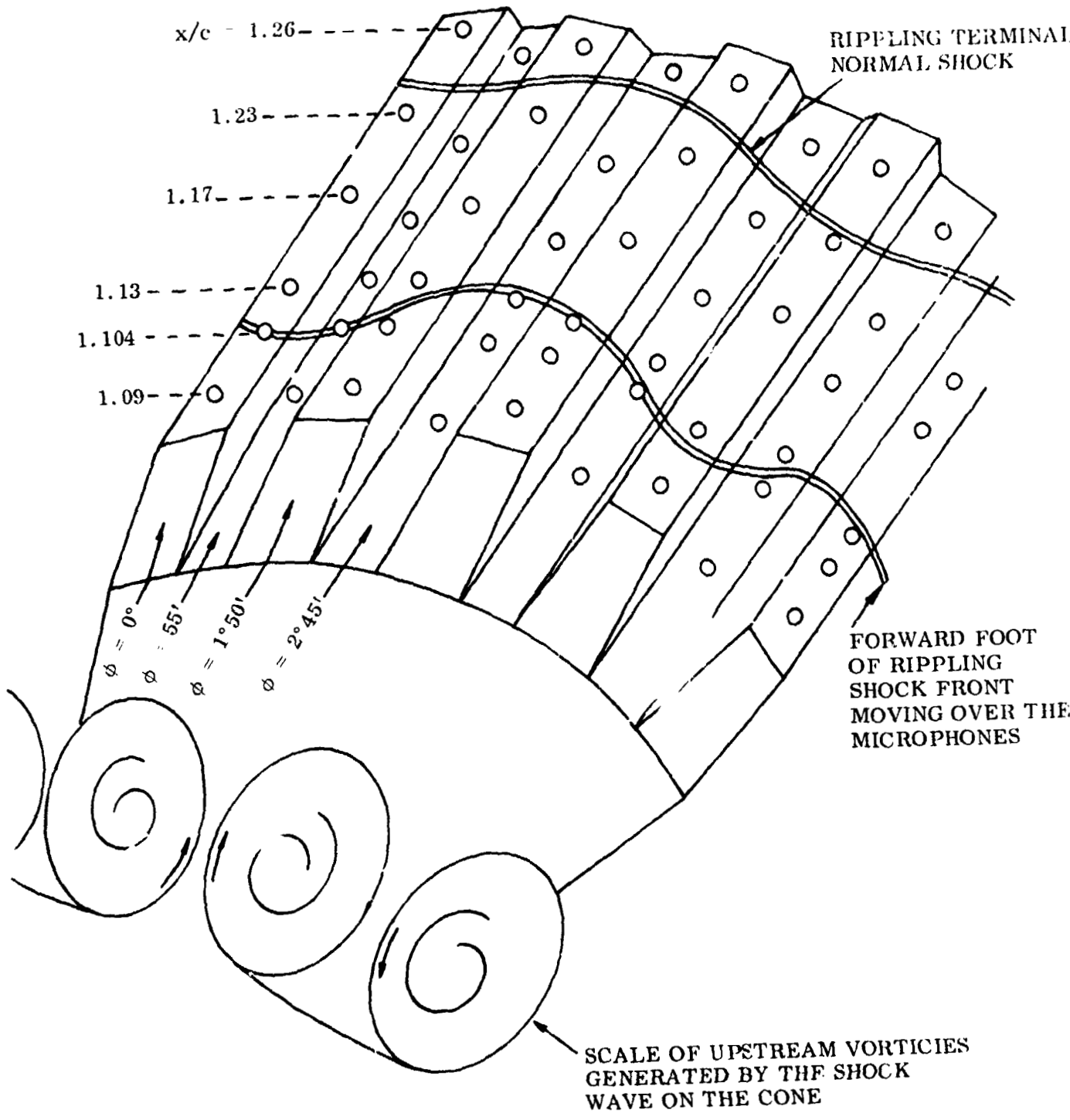

Fig. 23 Effect of Vortices on the Shock Front

vorticity generated at the shock-induced separation at the forward shoulder (as sketched in Fig. 23). The flow is accelerated and decelerated between vortices, causing the shock to take a more aft position in the accelerated flow regions.

The high-frequency noise from the boundary layer ahead of the shock is apparently convected away from the body surface in the separation under the forward lambda leg, and it is only the low-frequency content of the separated flow spectrum that shows coherence with the boundary-layer noise forward of the lambda (Fig. 24). This low-frequency noise is communicated via the shock oscillation driven by the upstream vorticity. Even thouth the flow within the separation pocket is three-dimensional rather than two-dimensional, two-dimensional theory seems to give a reasonable estimate of the lowest pocket resonance frequency. Trilling (Ref. 37) showed that a resonant condition can exist between shock oscillation and separated bubble growth. The present results (Fig. 25) show high coherence between shock and separated bubble noise at the lowest characteristic frequency predicted for the bubble using two-dimensional theory* (Ref. 5) (2760 cps in Fig. 25).

Thus, it appears that the vorticity generated within separated flow regions can set up a mechanism whereby very large axial correlation lengths could be realized for the fluctuating pressure environment of the body skin. The circumferential correlation, or lack thereof, is also to a high degree determined by this vorticity generated in the regions of shock boundary-layer interactions.

---

*It should be emphasized, however, that for certain critical flow geometries the two-dimensional approximation becomes completely inapplicable.

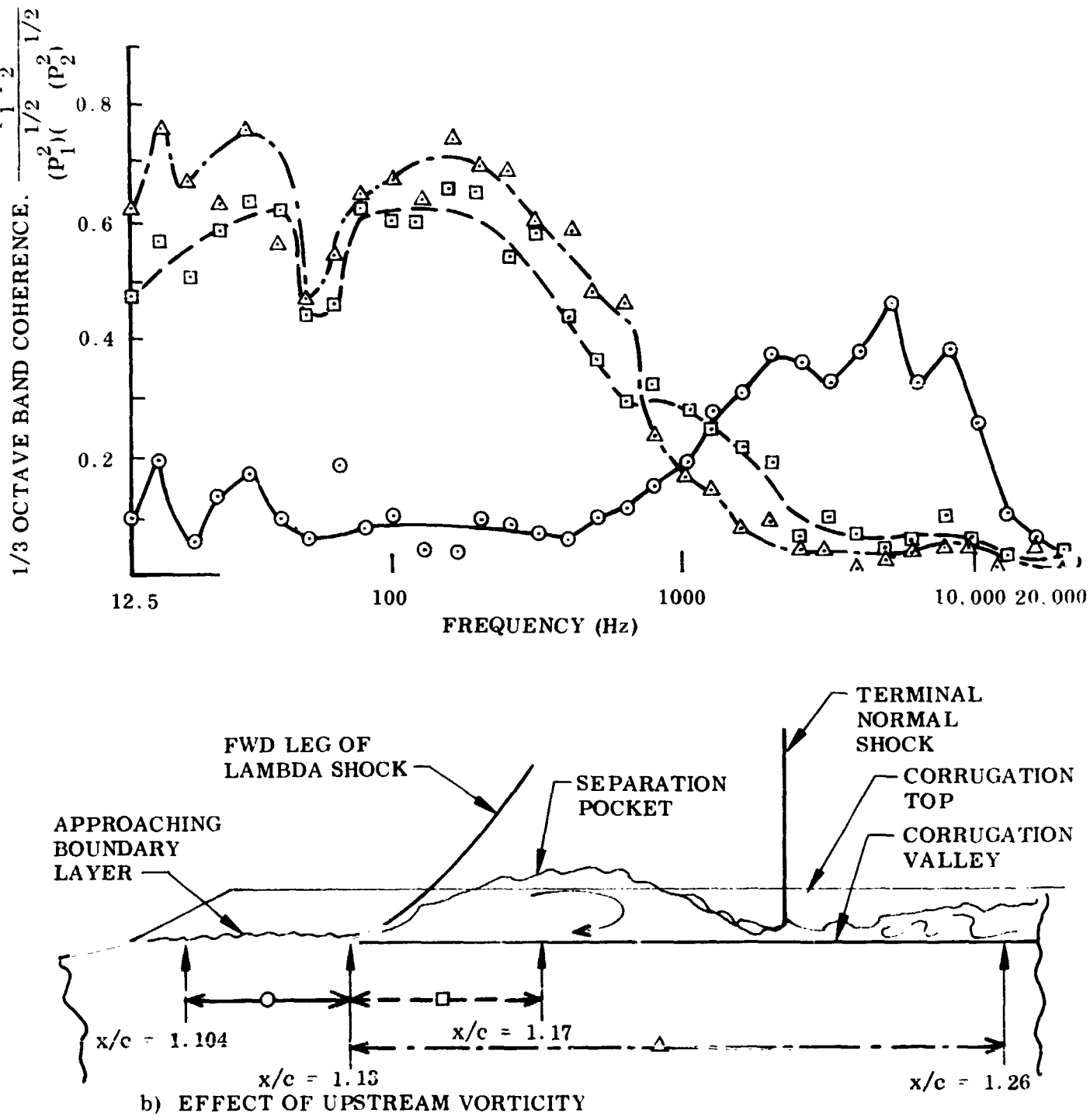

Fig. 24 Effect of Upstream Vorticity on Cross Correlation Spectra in the Vicinity of a Normal Shock at M = 0.8 and α = 2°

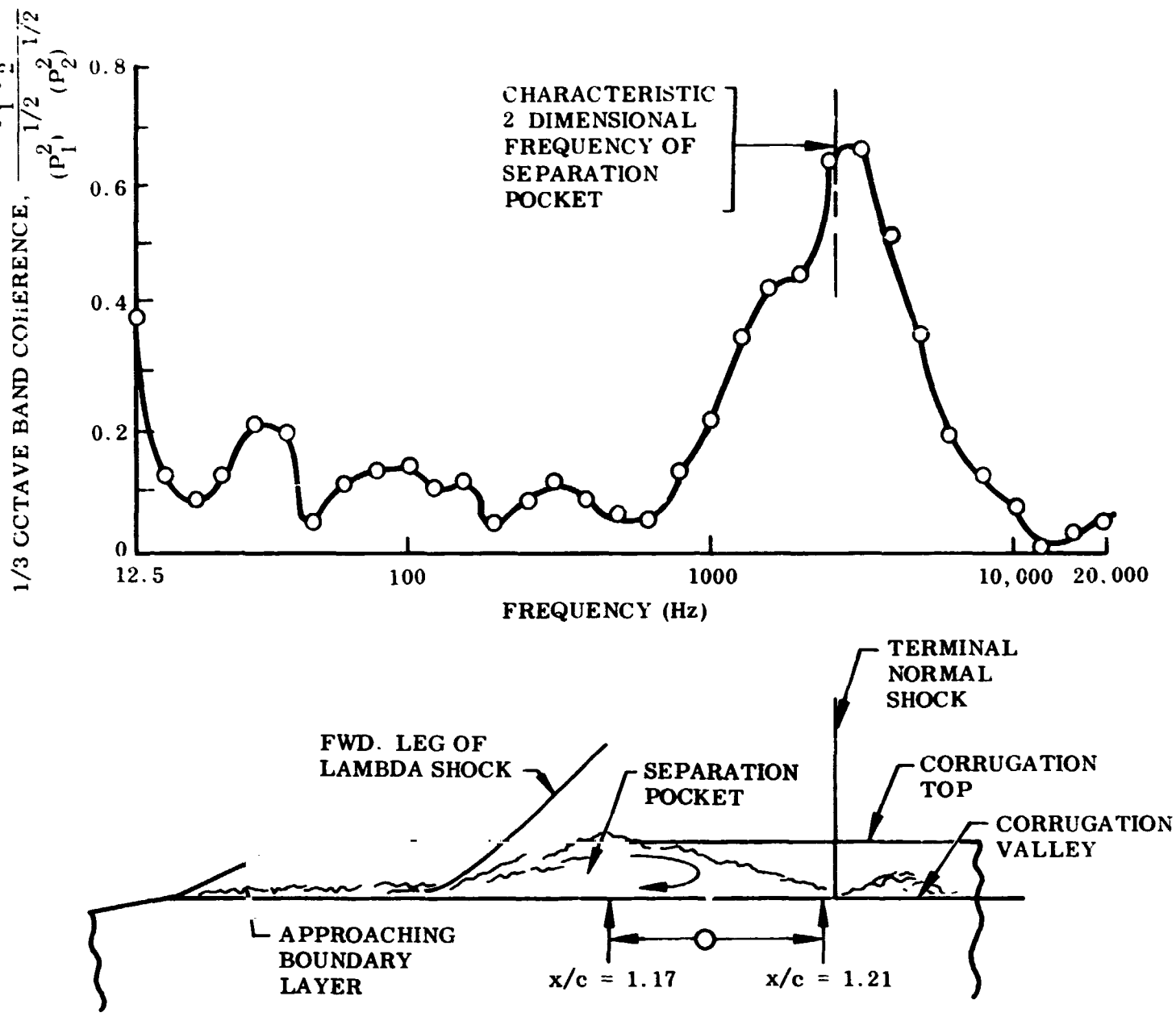

a) SEPARATION POCKET RESONANCE

Fig. 25 Effect of Separation Pocket Resonance on Cross Correlation Spectra in the Vicinity of a Normal Shock at M = 0.8 and α = 0

Section 6
CONCLUSIONS

A study of gust penetration loads on Saturn vehicles has revealed that available theories give unrealistic and often unconservative estimates. The lack of realism is due to the neglect of separated flow effects. An analytic theory is presented that uses actually measured static load distributions in a quasi-steady theory that includes the effects of separated flow and associated convective time lags.

It is found that sinusoidal gusts are potentially dangerous for Saturn V class elastic launch vehicles the critical structural loads being generated through the elastic vehicle response when the sinusoidal gust wave length gives resonance with the body bending. This critical gust response can be minimized changing the structural rigidity such that the gust induced bending moment is near minimum at the gust wavelengths giving resonance with the lower body bending modes. For simple missile geometries comprising a conical nose (payload shroud), a cylindrical body, and aft body fins, this design information can be expressed simply in form of a critical Strouhal number for the body bending frequency.

The Saturn V launch vehicles AS-505 through 508 are found to be aeroelastically stable throughout the atmospheric ascent. Their structural rigidity, however, is found to be far from optimal in the sense that it nearly maximizes the critical first bending mode resonant response to sinusoidal gusts. To determine whether this large gust response could impose intolerable structural loads is beyond the scope of the present investigation. It is clear, however, that elastic vehicle response to sinusoidal gusts may well produce the critical design loads.

Section 7
REFERENCES

1. L. E. Ericsson and J. Peter Reding, "Analysis of Flow Separation Effects on the Dynamics of a Large Space Booster," J. Spacecraft and Rockets, Vol. 2, No. 4, July-August 1965, pp. 481–490.

2. Lockheed Missiles & Space Company, Dynamics of Separated Flow over Blunt Bodies, by L. E. Ericsson and J. Peter Reding, Technical Summary Report 2-80-65-1, Contract NAS 8-5338, Sunnyvale, California, December 1965.

3. A. Gerald Rainey, "Progress on the Launch Vehicle Buffeting Problem," J. Spacecraft and Rockets, Vol. 2, No. 3, May-June 1965, pp. 289–299.

4. Lockheed Missiles & Space Company, Aeroelastic Characteristics of Saturn 1B and Saturn V Launch Vehicles, by L. E. Ericsson and J. Peter Reding, Technical Summary Report M-37-67-5, Contract NAS 8-11238, Sunnyvale, California, December 1967.

5. Lockheed Missiles & Space Company, Effects of Shock-Induced Separation, by L. E. Ericsson, J. P. Reding, and R. A. Guenther, Technical Summary Report L-87-69-1, Contract NAS 8-20354, Sunnyvale, California, June 1969.

6. Lockheed Missiles & Space Company, Attached Flow Gust Penetration Loads, by I. M. Scholnick, LMSC Report N-3C-69-1, Contract NAS 8-21459, Sunnyvale, Calif., January 1969.

7. Lockheed Missiles & Space Company, Analysis of the Experimentally Determined Aerodynamic Noise Environment for Three Nose-Cylinder Configurations, by J. Peter Reding and R. A. Guenther, LMSC Report N-3C-69-2, Contracts F04701-68-C-0061 and NAS 8-21459, Sunnyvale, Calif., October 1969.

8. Lockheed Missiles & Space Company, The Aeroelastic Characteristics of the Saturn V Launch Vehicle SA-505, by N. L. Davis, LMSC Report N-3C-69-2A, Contract NAS 8-21459, Sunnyvale, California, April 1969

9. Lockheed Missiles & Space Company, The Aeroelastic Characteristics of the Saturn-V Launch Vehicle SA-506 and an Updated SA-505, LMSC Report N-3C-69-2B, (Addendum to LMSC Report N-3C-69-2A), Contract NAS 8-21459, Sunnyvale, Calif., June 1969.

10. Lockheed Missiles & Space Company, The Aeroelastic Characteristics of the Saturn-V Launch Vehicle SA-507 for Launch Dates of 14 November and 16 November 1969, LMSC Report N-3C-69-2C (2nd Addendum to LMSC Report N-3C-69-2A), Contract NAS 8-21459, Sunnyvale, California, October 1969.

11. Lockheed Missiles & Space Company, The Aeroelastic Characteristics of the Saturn-V Launch Vehicle SA-508 for an April 1970 Launch Date, LMSC Report N-3C-69-2D, (3rd Addendum to LMSC Report N-3C-69-2A), Contract NAS 8-21459, Sunnyvale, California, October 1969.

12. Lockheed Missiles & Space Company, Report on Saturn I – Apollo Unsteady Aerodynamics, by L. E. Ericsson and J. Peter Reding, LMSC Report LMSC-A650215, Contract NAS 8-5338, Sunnyvale, California., February 1964.

13. Midwestern Research Institute, Study of Indicial Aerodynamic Forces on Multistage Space Vehicle Systems, Volume 1, Application of Theory to Basic Geometries and to the Saturn V, by W. D. Glauz and R. R. Blackburn, Final Report, 28 June 1962 – September 1968, Contract NAS 8-21167, MRI Project No. 3089-P.

14. H. C. Lester and H. G. Morgan, "Determination of Launch Vehicle Response to Detailed Wind Profiles," J. Spacecraft and Rockets, Vol. 2, No. 1, January-February 1965, pp. 62-67.

15. R. S. Ryan, T. Coffin, and L. L. Fontenot, "Dynamic Loads of a Launch Vehicle Due to Inflight Winds," Proceedings of the 3rd National Conference on Aerospace Meteorology, New Orleans, May 6–9, 1968, pp. 337–345.

16. C. J. Van Der Maas, "High-Speed Analysis of Wind-Induced Dynamic Loads on Vertically Rising Vehicles," J. Spacecraft and Rockets, Vol. 4, No. 5, May 1967, pp. 583–591.

17. Midwest Research Institute, Effects and Importance of Penetration and Growth of Lift on Space Vehicle Response, by R. R. Blackburn and A. D. St. John, NASA CR-326, Contract NAS 8-11012, November 1965.

18. R. L. Bisplinghoff, H. Ashley, and R. L. Halfman, Aeroelasticity, Cambridge, Mass., Addison-Wesley, 1955, pp. 418, 419.

19. C. R. Wells and H. P. Mitchell, "A Mathematical Model for Flexible Response of Uprated Saturn I In-Flight Winds," J. Spacecraft and Rockets, Vol. 5, No. 3., March 1968, pp. 313–320.

20. Lockheed Missiles & Space Company, Computer Program for Quasi-Steady Aero-Elastic Analysis, by N. L. Davis, LMSC Report LMSC M-37-67-3, Contract NAS 8-11238, Sunnyvale, California, December 1967.

21. R. R. Blackburn, "Responses of the Saturn V Space Vehicle to Inflight Wind Profiles," Proceedings of the 3rd National Conference on Aerospace Meteorology, New Orleans, La., May 6–9, 1968, pp. 327–336.

22. NASA, Terrestrial Environment (Climatic) Criteria Guidelines for Use in Space Vehicle Development, 1966 Revision, by G. E. Daniels, J. R. Scogins and O. E. Smith, NASA TM X-53328, May 1, 1966.

23. NASA, The Effect of Camber on the Aerodynamic Characteristics of a Body at a Mach Number of 2.01, by J. P. Gapcynski, NASA TM X-56, Sept. 1959.

24. J. P. Reding and L. E. Ericsson, "Loads on Bodies in Wakes," J. Spacecraft and Rockets, Vol. 4, No. 4, April 1967, pp. 511-518.

25. M. F. Gardner and J. L. Barnes, Transients in Linear Systems, Vol. 1, John Wiley & Sons, Inc., New York (1942)

26. J. G. Papadopoulos, "Wind Penetration Effects on Flight Simulation," Paper 67-609, AIAA Guidance, Control and Flight Dynamics Conference, Huntsville, Alabama, August 14–16, 1967

27. NASA,Sinusoidal Gust Criteria Guideline for Apollo Emergency Detection System Angular Rate Studies, by W. W. Vaughn, George C. Marshall Space Flight Center, Memo R-AERO-Y-31-64, 22 June 1964.

28. R. S. Ryan and A. C. King, "The Influential Aspects of Atmospheric Disturbances on Space Vehicle Design Using Statistical Approaches for Analysis," Paper 67-134, AIAA 5th Aerospace Sciences Meeting, New York, N.Y., January 23–26, 1967.

29. R. S. Ryan, J. R. Scoggins, and A. C. King, "Use of Wind Shears in the Design of Aerospace Vehicles, J. Spacecraft and Rockets, Vol. 4, No. 11, November 1967, pp. 1526–1532.

30. C. F. Coe, NASA Ames Research Center, Private Communication of Currently Unpublished data.

31. H. L. Chevalier, NASA Ames Research Center, Private Communication of Currently Unpublished data.

32. A. Roshko and G. J. Thomke, "Observations of Turbulent Reattachment Behind an Axisymmetric Down-Stream Facing Step in Supersonic Flow," AIAA Journal, Vol. 3, No. 6, Jan. 1966, pp. 975–980.

33. J. J. Ginoux, On Some Properties of Reattaching Laminar and Transitional Flows, von Karman Institute, TN 53, Sep 1969.

34. H. T. Uebelhack, Turbulent Flow Separation Ahead of Forward Facing Steps in Supersonic Two-Dimensional and Axi-symmetric Flows, von Karman Institute, TN 54, Jul 1969.

35. Lockheed Missiles & Space Company, The Aeroelastic Characteristics of the Saturn IB Launch Vehicle with Biconic Payload Shroud, by L. E. Ericsson, N. J. French, and R. A. Guenther, LMSC Report M-37-67-1, Contract NAS 8-11238, Sunnyvale, Calif., July 1967.

36. L. E. Ericsson, "Aeroelastic Instability Caused by Slender Payloads, J. Spacecraft and Rockets, Vol. 4, No. 1, Jan. 1967. pp. 65–73.

37. L. Trilling, "Oscillatory Shock Boundary Layer Interaction," J. Aeronautical Sciences, Vol. 25, No. 5, May 1958, pp 301–304.

Section 8
RECOMMENDATIONS FOR FUTURE STUDY

The performed study has demonstrated the need for more realistic evaluations of gust penetration effects than those provided by generally available theories. This is especially true when shock-boundary layer interactions and flow separations are present. Both gross bending mode response and high frequency panel response are highly affected by separated flow effects. As the upcoming space shuttle with its dual vehicle launch mode will present even more shock interactions and boundary layer separations than the Saturn V launch vehicle, and will provide more possibilities for several degrees of freedom elastic response, it is urgent that theoretical methods be developed that do not completely neglect the existence of these "non-nice" flow phenomena, which all experiments have shown to have dominant effects on both rigid and elastic body vehicle dynamics. The fallacy in relying on dynamic tests to give the needed information was proven for the early Saturn I boosters.

The developed theory should be checked further by special dynamic tests. However, the results obtained so far give reason for confidence, and work should be started now to extend the theory for application to the more complicated flow fields existing on the various candidate space shuttle configurations.

Appendix A
NOMENCLATURE

a	Speed of sound, m/sec
A	Cross-sectional area, m^2
A_n and B_n	Parameters defined in Eqs. (4.54) and (4.55)
B	Parameter defined in Eq. (4.33)
c	Reference length (maximum body diameter) m
C_{n_i} and C_n	Summation coefficients defined in Eqs. (4.41), (4.42), and (4.42A)
D	Aerodynamic damping derivative defined in Eq. (4.31)
E_n and F_n	Summation coefficients defined in Eqs. (4.56) and (4.57)
f	Gust function of inertial space coordinate X
g and G	Gust functions of time defined in Eqs. (4.33), (4.34), and (4.35)
i	The imaginary number $\sqrt{-1}$
I	Momentum, kg-sec
K	Aerodynamic stiffness derivative defined in Eq. (4.31)
L_b, L_b^* and L_g	Body length, body characteristic length, and gust wavelength, m
L	Lift, kg. coefficient $C_L = L/(\rho U^2/2)S$
$\tilde{m}$	Generalized mass, $kg\text{-}sec^2/m$
M	Mach number $M = U/a$
M_A and m_A	Axial force generated pitching moment, Kg-m. Coefficient $C_{m_A} = M_A/(\rho U^2/2)Sc$
M, N	Maximum number of summation terms, Eq. (4.31)

N and n	Normal force, Kg: Coefficient $C_N = N/(\rho U^2/2)S$
P(t)	Generalized force, kg or kg-m/m, defined in Eq. (4.18)
p	Aerodynamic pressure, kg/m^2: Coefficient $C_p = (p - p_\infty)/(\rho U^2/2)$
q (t)	Amplitude, m. of normalized bending deflection, φ (x) q(t)
r	Body (cross section) radius, m
s	Laplace variable, Eq. (4.36)
$\mathcal{S}$(t)	Unit step function
S	Reference area, m^2 : $S = \pi c^2/4$
S*	Critical Strouhal number, Eq. (5.5)
t, t', t*	Time, sec
U	Vehicle velocity, m/sec
W_g, w_g	Gust velocity normal to vehicle path, m/sec (Eq. (4.14) and Fig. 6
X	Inertial space coordinate, m (Figs. 6 and 7)
x	Body fixed coordinate, m (Fig. 6)
Y	Inertial space coordinate, m (Fig. 6)
y	Body fixed lateral deflection due to bending, m (Fig. 6)
α	Angle of attack, radians or degrees
β	Angular measure of lateral translation, radians or degrees
β_E	Gimbel engine deflection, radians
Δ	Amplitude or increment
ϵ	Closeness-to-resonance parameter, Eq. (4.50)
ζ	Structural damping, fraction of critical
ζ_T	Total damping, fraction of critical, Eq. (4.34)
θ	Bending body slope, radians or degrees
κ	Time lag parameter defined in Eq. (4.8)

μ_g	Ramp-gust slope, Eq. (4.16): $\mu_g = 4U/L_g$
ν_{max}	Maximum number of sinusoidal gust cycles o. given wavelength (Fig. 20)
ρ	Air density, kg-sec^2/m^4
σ	Whole number, Eqs. (5.3) – (5.6)
$\varphi(x)$	Distribution of normalized bending mode deflection, φ (x) q(t)
ψ	Phase lag, radians of degrees
ω	Free-free bending frequency, radians/sec
ω_g	Sinusoidal gust frequency, radians/sec, Eq. (4.16) $\omega_g = 2\pi U/L_g$

Subscripts

a	attached flow
b	body
g	gust
i	numbering subscrip[illegible]y station
L	local conditions
n	numbering subscript, Eq. (4.42a)
s	Separated flow
T	Total
u	Upstream communication
o	Gust entry or vehicle apex
∞	Undisturbed flow

Superscripts

i	induced, e.g., = separation induced normal force
–	barred quantities, e.g., $\bar{x}_i$ or $\bar{\bar{W}}_g$, denote integrated space or time averages.
^	"roofed" symbols denote Laplace transformed functions

Differential Symbols

$$\varphi'(x) = \frac{\partial \varphi}{\partial x}$$

$$\dot{Y}(t) = \frac{\partial Y}{\partial t} \qquad \ddot{q}(t) = \frac{\partial^2 q}{\partial t^2}$$

$$C_{N_\alpha} = \frac{\partial C_N}{\partial \alpha}$$

Appendix B

AEROELASTIC CHARACTERISTICS OF SATURN-V LAUNCH VEHICLES AS-505 THROUGH AS-508

The most severe aerodynamic environment encountered by the Saturn V Launch vehicles occurs at transonic Mach numbers in the flight regime of maximum dynamic pressure. Large regions of separated flow exist on the vehicle, causing highly non-linear loads which strongly influence the vehicle damping. The quasi-steady method described in Refs. 12 and 20, which includes the effects of separated flow and employs experimentally obtained static load distributions, was applied to determine the aeroelastic characteristics of the Saturn-V launch vehicles AS-505 through AS-508 (Refs. 8-11). The results are summarized here.

The Saturn-V vehicle geometry shown in Fig. B-1 and corresponding static loads apply to the current vehicles as well as the previous Saturn-V flight vehicles AS-501, AS-502, AS-503, and AS-504 (Ref. 23). Using flight vehicle AS-504 as a reference, the bending mode shapes of the present vehicles AS-505 through AS-508 are shown in Fig. B-2. The corresponding aerodynamic damping in percent of critical is shown as a function of Mach number in Fig. B-3, a, b, and c for $\alpha = 0$, $\alpha = 4°$, and $\alpha = 8°$ respectively. The results indicate that the present vehicle, as AS-504 earlier, will be dynamically stable throughout atmospheric ascent.

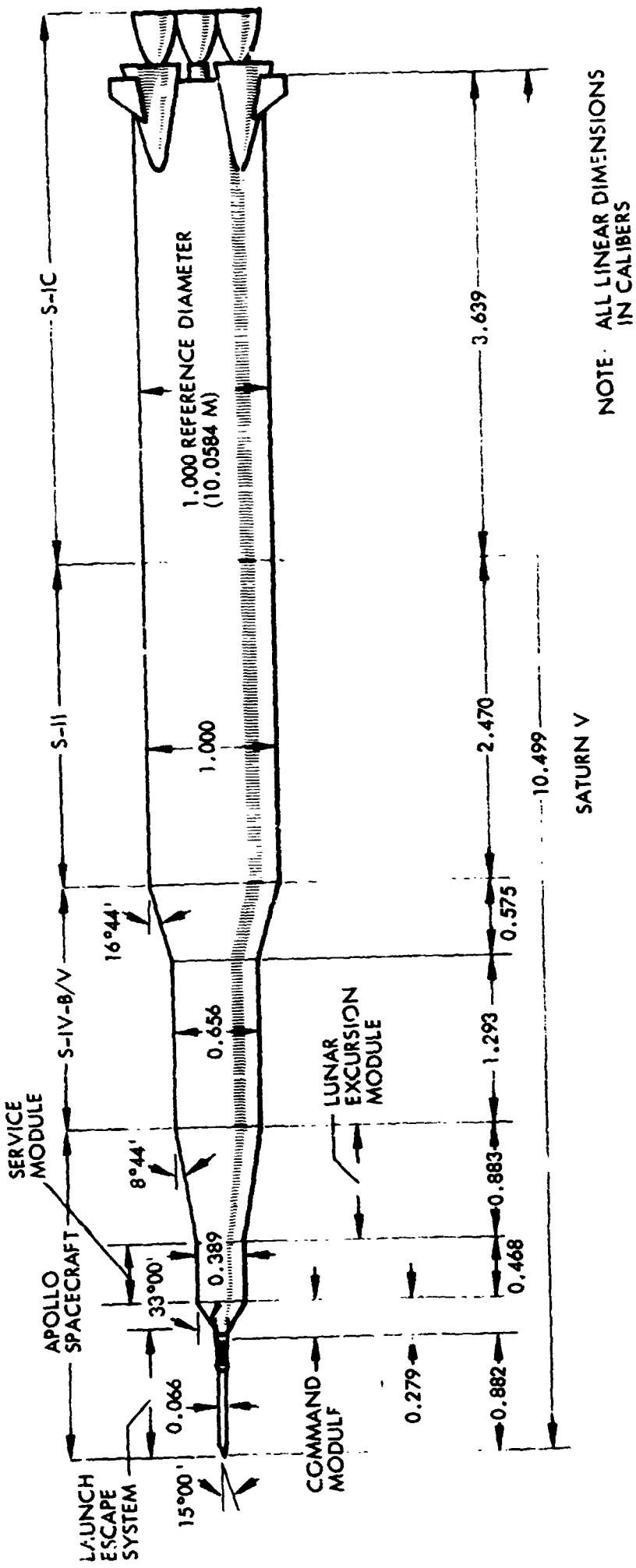

Fig. B-1 Saturn-V Vehicle Geometry

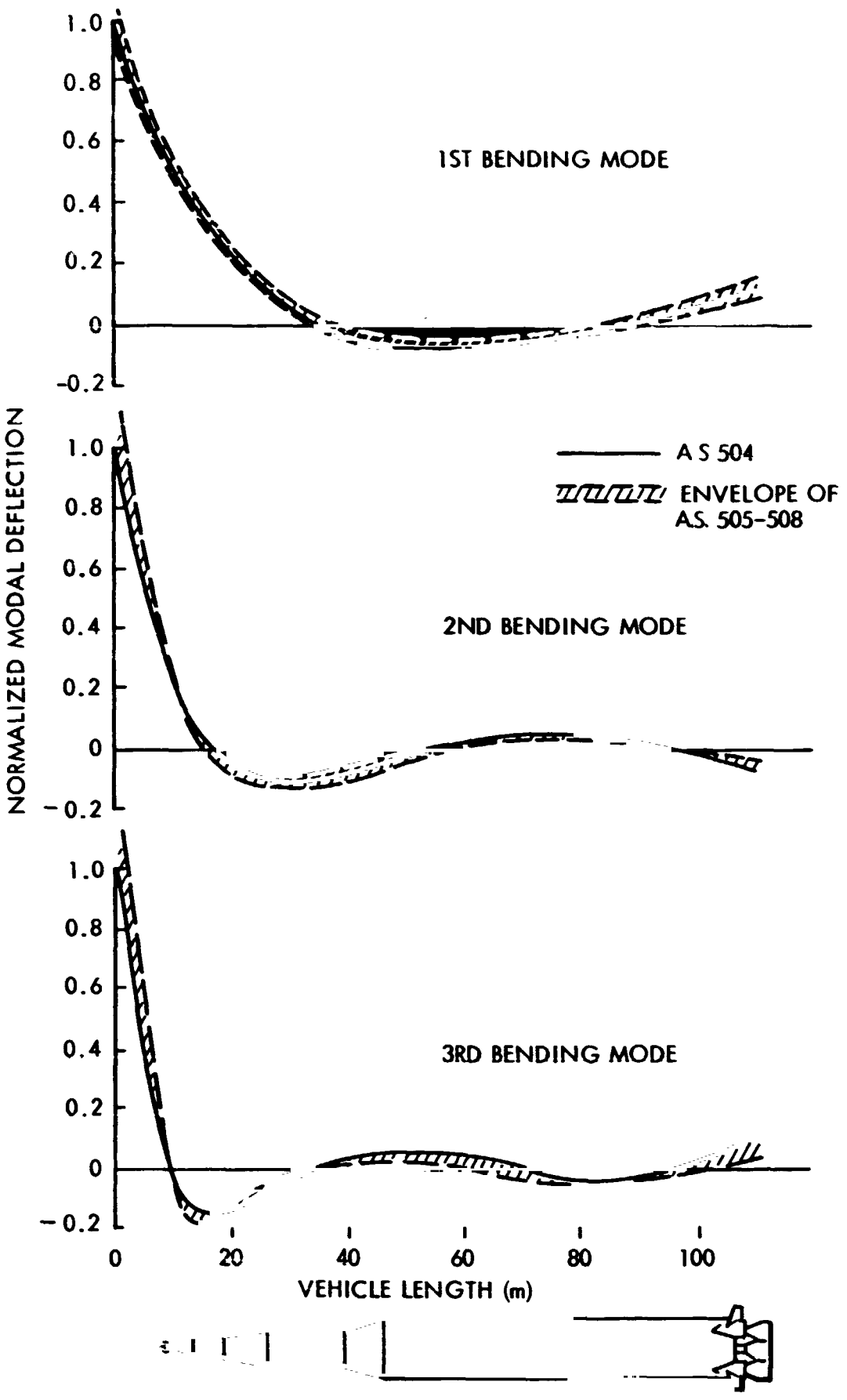

Fig. B-2 Bending Mode Shapes for Vehicles AS-505 through AS-508 Compared to the AS-504 Mode Shapes

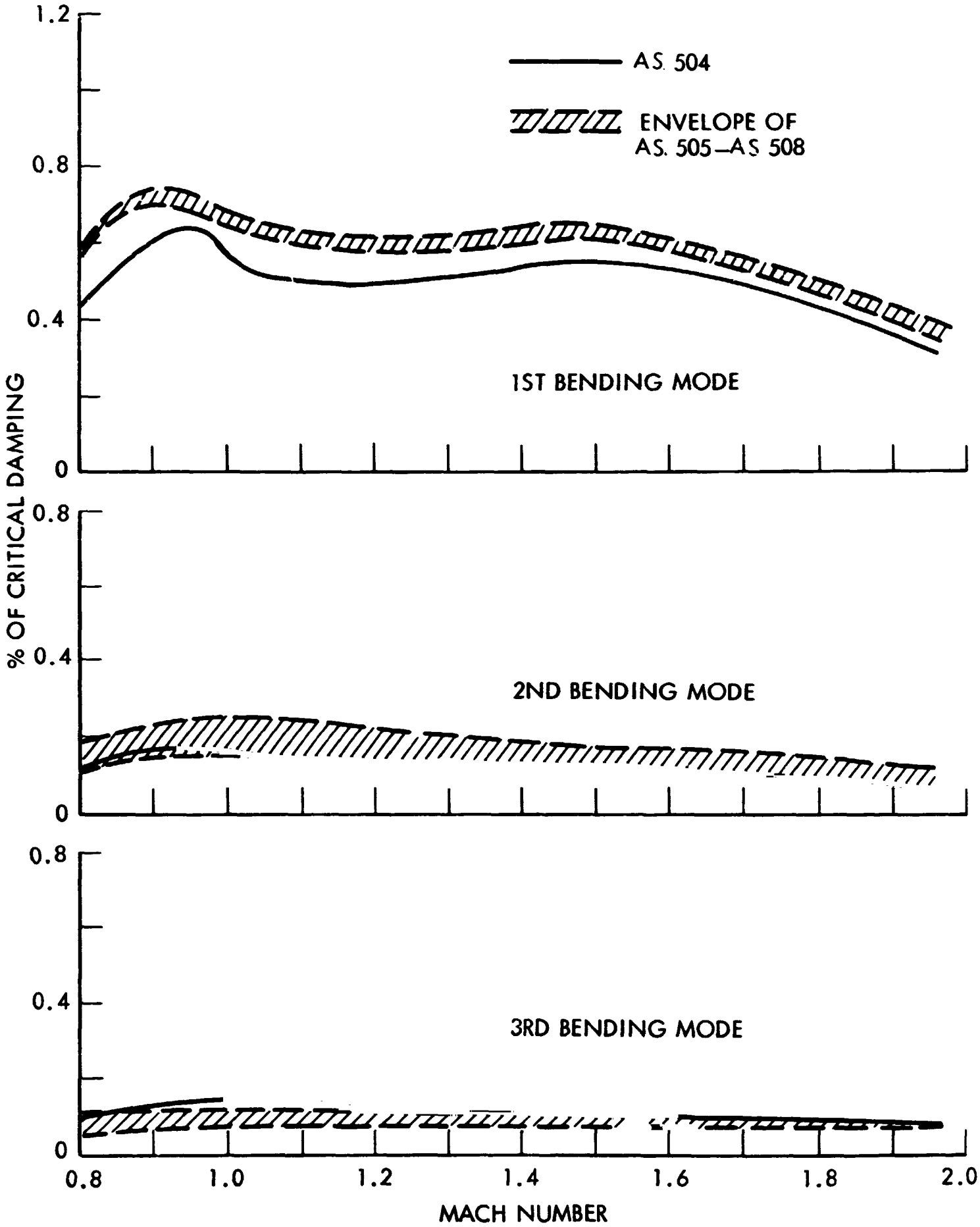

Fig. B-3a Aerodynamic Damping of Vehicles AS-505 through AS-508 Compared to the AS-504 Damping (α = 0)

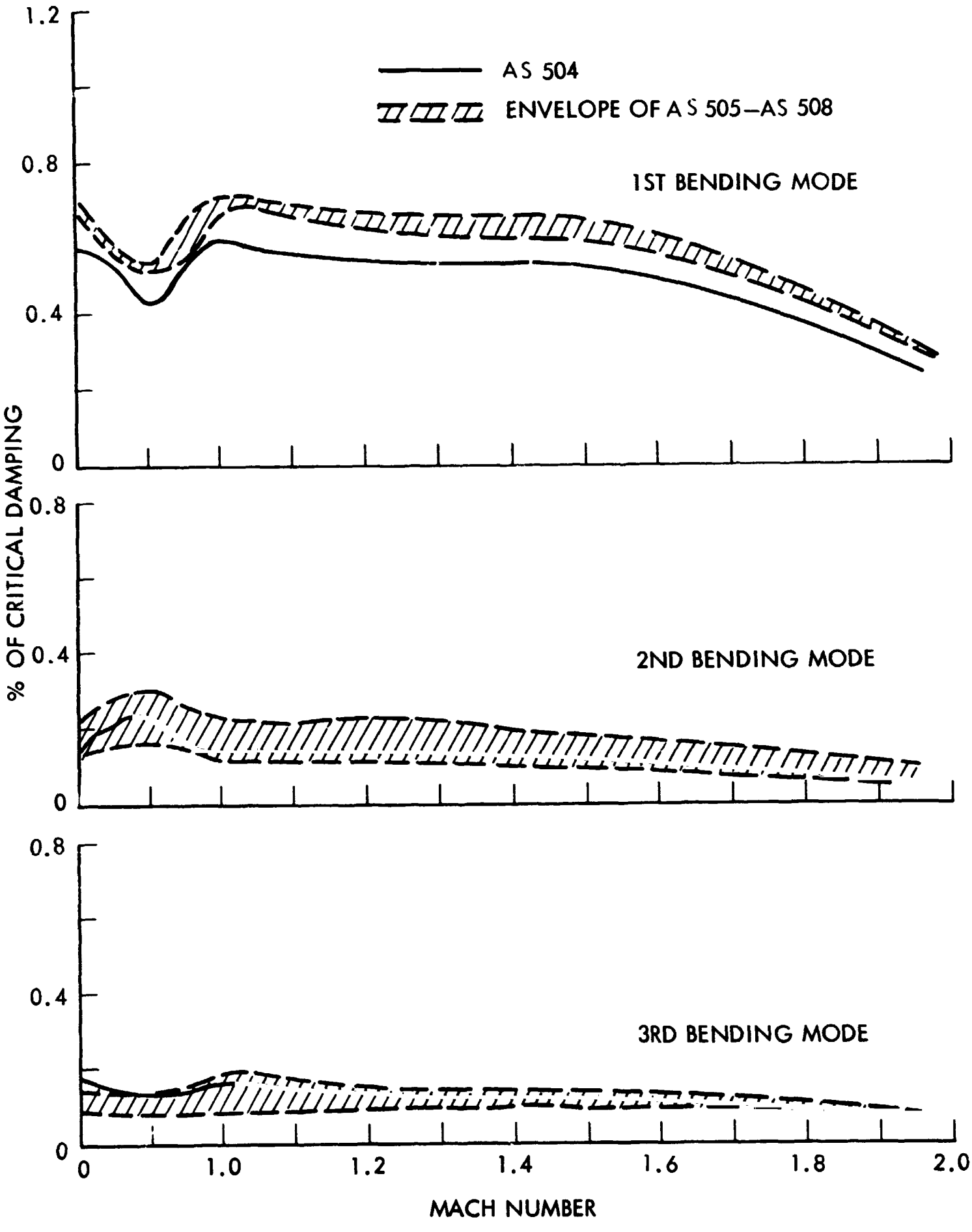

Fig. B-3b Aerodynamic Damping of Vehicles AS-505 through AS-508 Compared to the AS-504 Damping (α = 4°)

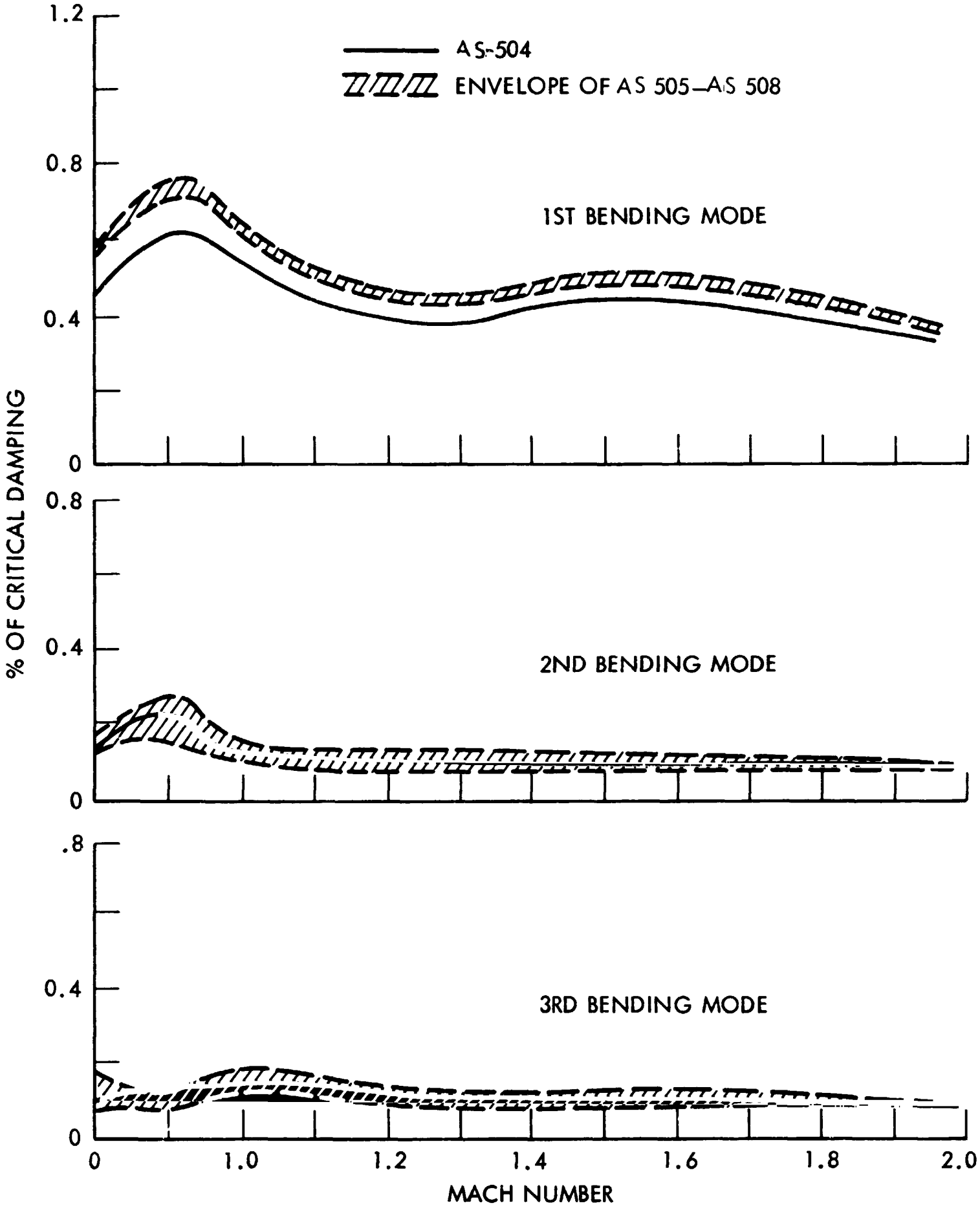

Fig. B-3c Aerodynamic Damping of Vehicles AS-505 through AS-508 Compared to the AS-504 Damping (α = 8°)